UNIVERSITY OF ROCHESTER
LABORATORY FOR LASER ENERGETICS

Volume 59
April–June 1994
DOE/SF/19460-36

LLE Review

Quarterly Report

About the Cover:

Scientist Robert Kremens is shown inserting one of the 960 scintillator-photomultiplier neutron detectors into the time-of-flight spectrometer array "MEDUSA." The array is being constructed in a separate diagnostic room 20 m from the center of the OMEGA Upgrade target chamber. Also visible in the photograph are the computer-controlled data acquisition system and one of several racks of electronics. This diagnostic will measure fuel areal density and ion temperature for pure deuterium target implosions.

The work described in this volume includes current research at the Laboratory for Laser Energetics, which is supported by New York State Research and Development Authority, the University of Rochester, the U.S. Department of Energy Office of Inertial Confinement Fusion under Cooperative Agreement No. DE-FC03-92SF19460, and other agencies.

For questions or comments, contact James P. Knauer, *Editor*, Laboratory for Laser Energetics, 250 East River Road, Rochester, NY 14623-1299, (716) 275-2074.

Printed in the United States of America
Available from
National Technical Information Services
U.S. Department of Commerce
5285 Port Royal Road
Springfield, VA 22161

Price codes: Printed Copy A04
Microfiche A01

UNIVERSITY OF ROCHESTER
LABORATORY FOR LASER ENERGETICS

Volume 59
April–June 1994
DOE/SF/19460-36

LLE Review

Quarterly Report

UR LLE

Contents

In Brief

This volume of the LLE Review, covering the period of April–June 1994, contains articles on surface characterization by atomic force microscopy; electron acceleration with intense laser field; spatial intensity variations induced by nonlinear beam propagation; backlighting of implosion targets exhibiting mix; and the use of cosmic rays to monitor large, multielement detectors. Four of these articles—surface characterization; nonlinear beam propagation; backlighting of mixed targets; and monitoring of the MEDUSA detector array—are directly related to the OMEGA Upgrade, which is currently under construction.

Highlights of the research presented in this issue are

- The effect on water-induced surface damage on thin-film coatings is studied with an atomic-force microscope. An experiment was conducted with Y_2O_3 coatings on BK-7 glass. Pyramidal growth features that irreversibly modify the columnar-growth structures have been observed.

- The acceleration of electrons from an underdense gas in the focal volume of a high-intensity laser has been observed. First-order relativistic effects are expected to occur at laser intensities of 10^{18} W/cm^2. The longitudinal acceleration of electrons from the magnetic-field term in the Lorentz force has been observed for the first time.

- The effect of stimulated rotational Raman scattering and propagation through a spatial filter at various vacuum pressures on the spatial uniformity of a high-power laser beam is reported. These two experiments were conducted in support of the OMEGA Upgrade design and construction. Transverse modulational instabilities were observed for both of the above experiments with the OMEGA laser. The data agree with previous work conducted in the field.

- The ability to diagnose an imploding target that is subject to mixing with an x-ray backlighter is calculated. The expected images from targets exhibiting mixing at the fuel-pusher interface that are either doped with a high-Z element or undoped CH shells show the utility of using a monochromatic backlighter to study this interface. The simulations indicate that data from this diagnostic technique will be used to deduce both the low-order nonuniformity and compression of the final core.

- A large scintillator array is being built to measure the secondary neutron emission from ICF targets. The ability to monitor the individual channels of this diagnostic is important to the interpretation of the data. A technique that uses cosmic rays to determine the status of each scintillator-photomultiplier detector is shown to provide the necessary information to evaluate the performance of the MEDUSA diagnostic.

James P. Knauer
Editor

Atomic Force Microscopy Observation of Water-Induced Morphological Changes in Y_2O_3 Monolayer Coatings

Environmental stability studies for thin-film coating materials employed on the upgraded OMEGA laser system are essential for defining acceptable air humidity levels and their control, as well as for facilitating proper thin-film coating design of long-term-use OMEGA laser optics. Moisture penetration into porous, dielectric thin-film coatings causes generally undesirable changes in the film's optical performance parameters—a fact that has been well known for some time now.[1,2] The major effects previously observed and studied in this regard are shifts in the transmission characteristics of narrow-band filters,[3,4] caused by the replacement of air with a 1.3-index medium inside the pores; enhanced absorption in the IR water band;[5] and changing mechanical stress (either compressive or tensile)[6] that renders difficult maintaining stringent wavefront-error requirements on reflective components. Thermal annealing,[7] ion bombardment, and, more generally, preparing coatings with dense-packing structure are among the methods devised in combating water effects in dielectric films.

In addition to these macroscopic effects, certain narrow-band filters also showed microscopic morphology modifications upon water penetration. These changes took the form of circular patches that remained unaffected even by a 4-h vacuum treatment of the dielectric filter stack at 200°C.[3] To our knowledge, no detailed, submicron resolution studies of such patterns were performed to date, and no fundamental insight into the growth mechanism of such patterns exists.

In this work, Y_2O_3 monolayer coatings, grown by Alpine Research Optics Inc., Boulder, CO, were used to examine AFM-resolution morphological changes caused by both a standard laboratory environment and artificial, accelerated testing in 100% relative humidity and also by droplet seeding.

Experimental Method

BK-7 glass substrates served as support for electron-beam-evaporated, 1-μm-thick, single-layer Y_2O_3 coatings. During evaporation, substrates were held at 300°C. After shipment, samples were stored in conventional, unsealed containers. In as-received condition, the films showed no evidence of moisture penetration; however, after 2-months' exposure to a fluctuating-humidity laboratory environment, reaching sporadic humidity episodes with up to 90% relative humidity, first signs of water-penetration-induced morphology changes were observed. After an additional two months, steady-state, moisture-penetration patterns developed.

Sample microscopy was carried out on a Nanoscope III (Digital Instruments, Inc.) Atomic Force Microscope using several probes, depending on sample average-surface-roughness conditions. On smooth areas with peak-to-valley variations <500 nm and lacking steep structural features, standard silicon nitride (Si_3N_4) probes proved adequate. For steep-height-gradient situations, etched silicon probes of high aspect ratio were necessary to avoid "surface-probe convolution" imaging. The Y_2O_3 surface proved to be quite stable even after hard engagement of the probe tip, and no special measures seemed necessary to prevent surface modification by the probe. A challenge did arise from the "stickiness" of the probes to water-modified sample areas, which we attributed to excessive electrostatic charging. Adjustments to the microscope feedback loop and reducing the scanning speed were successful countermeasures in this case. Microscope resolution was limited by residual system vibration noise that remained after isolation of the entire AFM/optical microscope monitor assembly on commercial vibration-isolation mounts. Cleaved-mica reference surfaces were readily imaged at atomic-scale resolution in this microscope-mounting configuration.

Artificial seeding of sample surfaces with de-ionized, distilled H_2O (18 MΩ/cm) was accomplished using a micropipette dispenser with 40-nl resolution. In the standard laboratory environment, such small water volumes evaporate from the sample surface within tens of seconds.

Moisture-Penetration Patterns

Resolving the earlier-reported, circularly symmetrical, water-penetration islands at increased resolution, one finds each island to contain a pronounced, central, pyramidal feature (occasionally split into twins or a closely packed multitude of

pyramids). Typical examples of such features are depicted in Figs. 59.1(a)–59.1(c). Their height above the adjacent film surface reaches 3 μm, and lateral extensions of up to 10 μm have been encountered. These pyramids are surrounded by a pronounced concentric-ring pattern varying in diameter from 10 to 100 μm [Figs. 59.2(a)–59.2(d)] and in width from 5 to 30 μm. We surmise that variations in ring sizes represent various developmental stages in ring formation.

When the features are small, i.e., at the early stages of the process, the concentric ring is not yet clearly isolated from the central feature and contains a high density of tiny pyramids [Fig. 59.2(a)]. Upon further development, the ring separates from the central feature, leaving a concentric region with two distinct spatial and structural characteristics [Figs. 59.2(b) and 59.2(c)]. At the same time, small pyramids in the central region merge into the larger, micron-scale central pyramid [Figs. 59.1(b) and 59.1(c)].

Analyzing the region between the central pyramid and the ring, one finds the following radial subdivision: In the immediate vicinity of the central pyramid a patchwork of islands

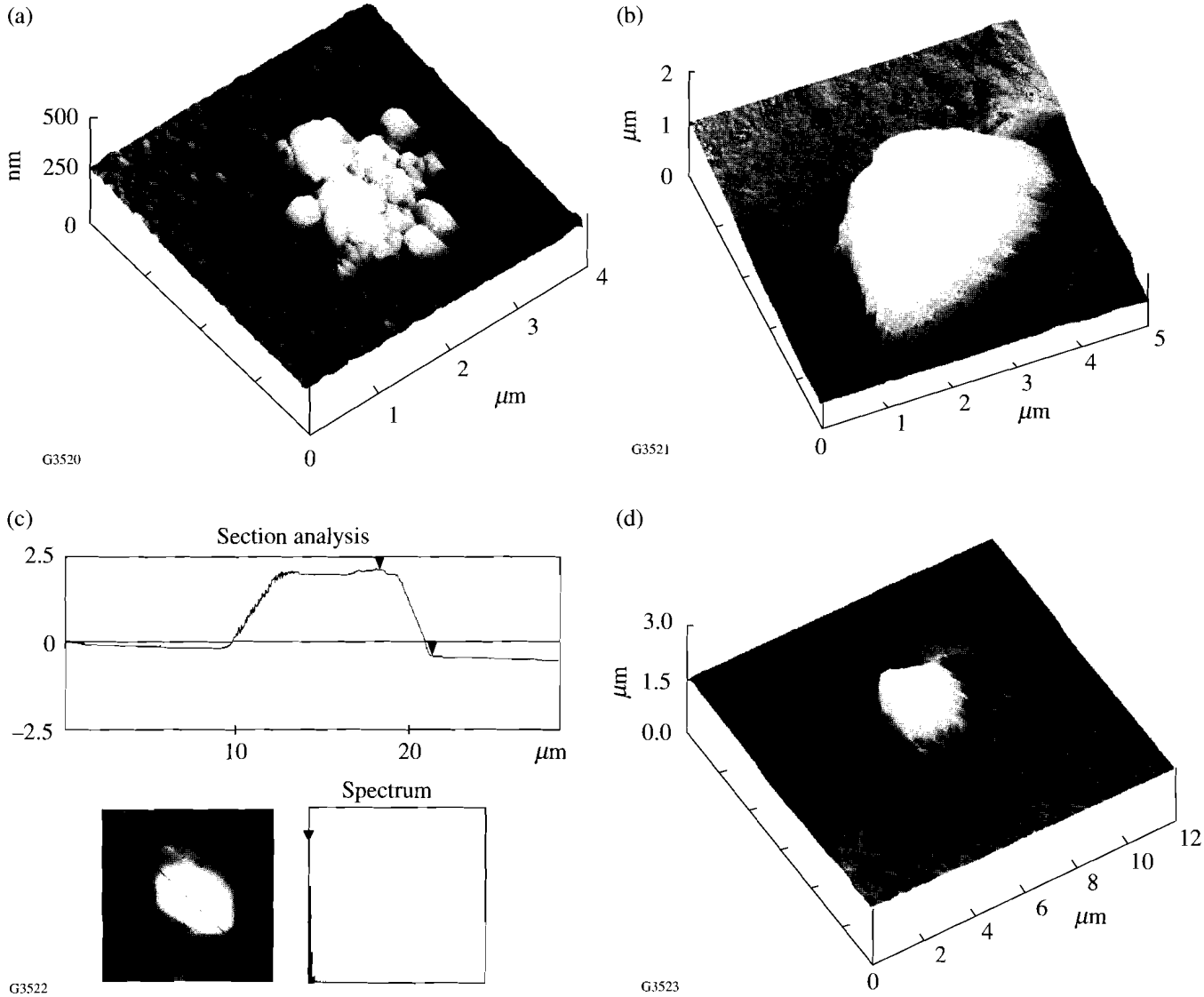

Figure 59.1
(a) Early developmental stage of a water-penetration-island central feature; small pyramids have already formed but have not yet merged. (b) Monolithic pyramidal structure with 5-μm base and 1-μm height typically found in the center of well-developed water-penetration islands. (c) Cross-sectional scan through a fully developed, 10-μm base pyramid. (d) Lower magnification view of pyramid in (b), allowing view of surrounding zone.

exists that differ from one another in both rms roughness and average height [Fig. 59.1(d)], while near the inner edge of the ring is a zone where the columnar film structure is undergoing coalescence. A similar zone of columnar coalescence is also found around the outer edge of the ring. In fact, columnar coalescence appears to be a global film process that we observed with a reduced time constant in unaffected film areas as well. At this time, the difference in rate constants between coalescence in water-penetration island areas and coalescence in "unaffected" areas appears to be a factor of 2 to 3.

Near the central pyramid, the island topography [Fig. 59.1(d)] comprises up to 100-nm height variations among islands, with rather-smooth-surface islands always being depressed in height relative to rough-surface islands. Figure 59.3(d) shows a head-on view of the columnar structure in one of the smooth

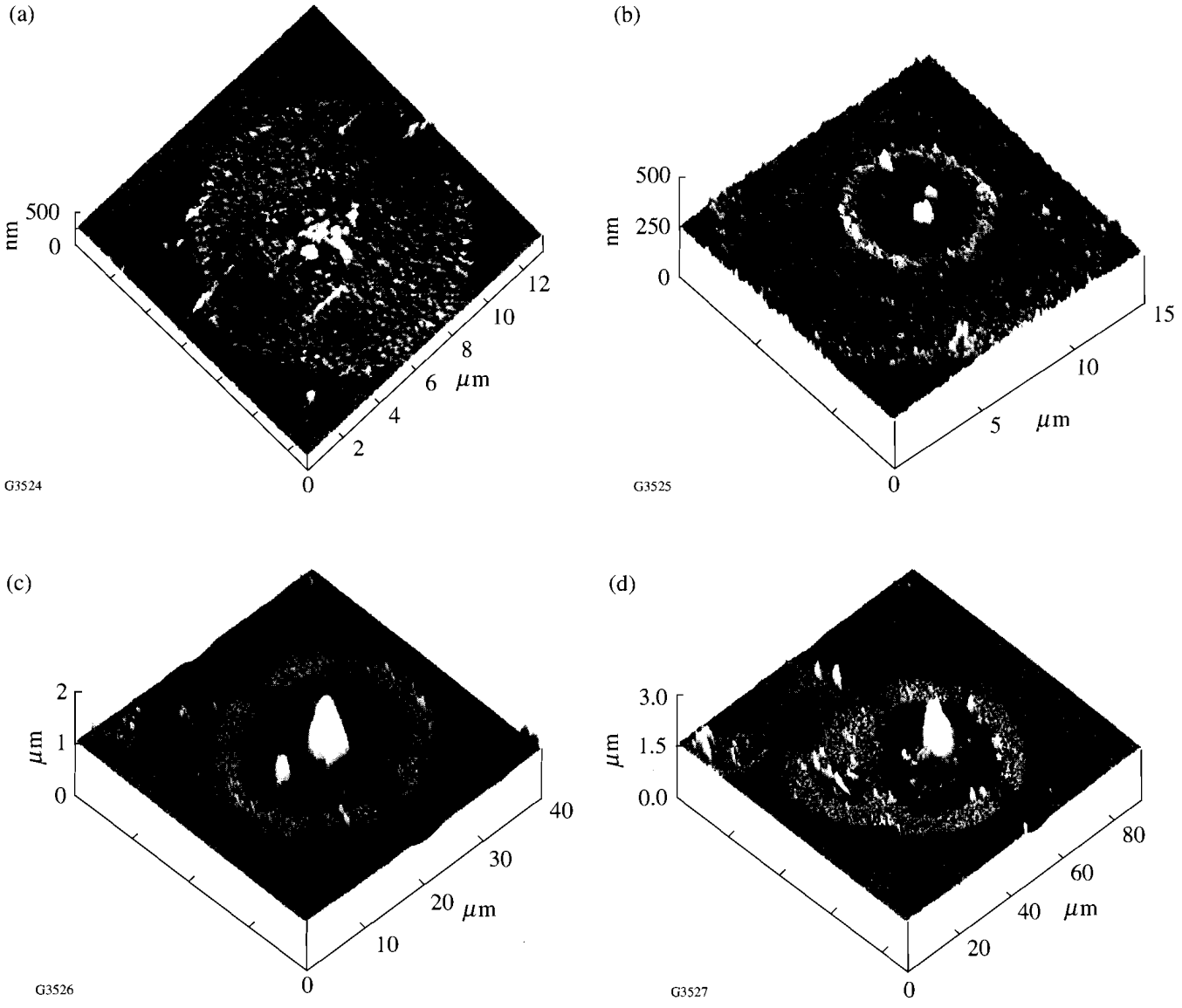

Figure 59.2
(a) View of the early stage of pattern formation: the ring (12-μm outer diameter) has not yet separated from the central feature. (b) View of ring separation in progress: the central feature is clearly developed, and a "dead-zone" between ring and central feature has evolved (18-μm) ring diameter. (c) Steady-state pattern of fully developed central pyramid, ring, and intermediate zone, which contains randomly distributed, rough, and very smooth patches with height variations of up to 100 nm. (d) Very-large, >60-μm-diam, water-penetration pattern with asymmetric shape resulting from the merger of two adjacent patterns at different developmental stages.

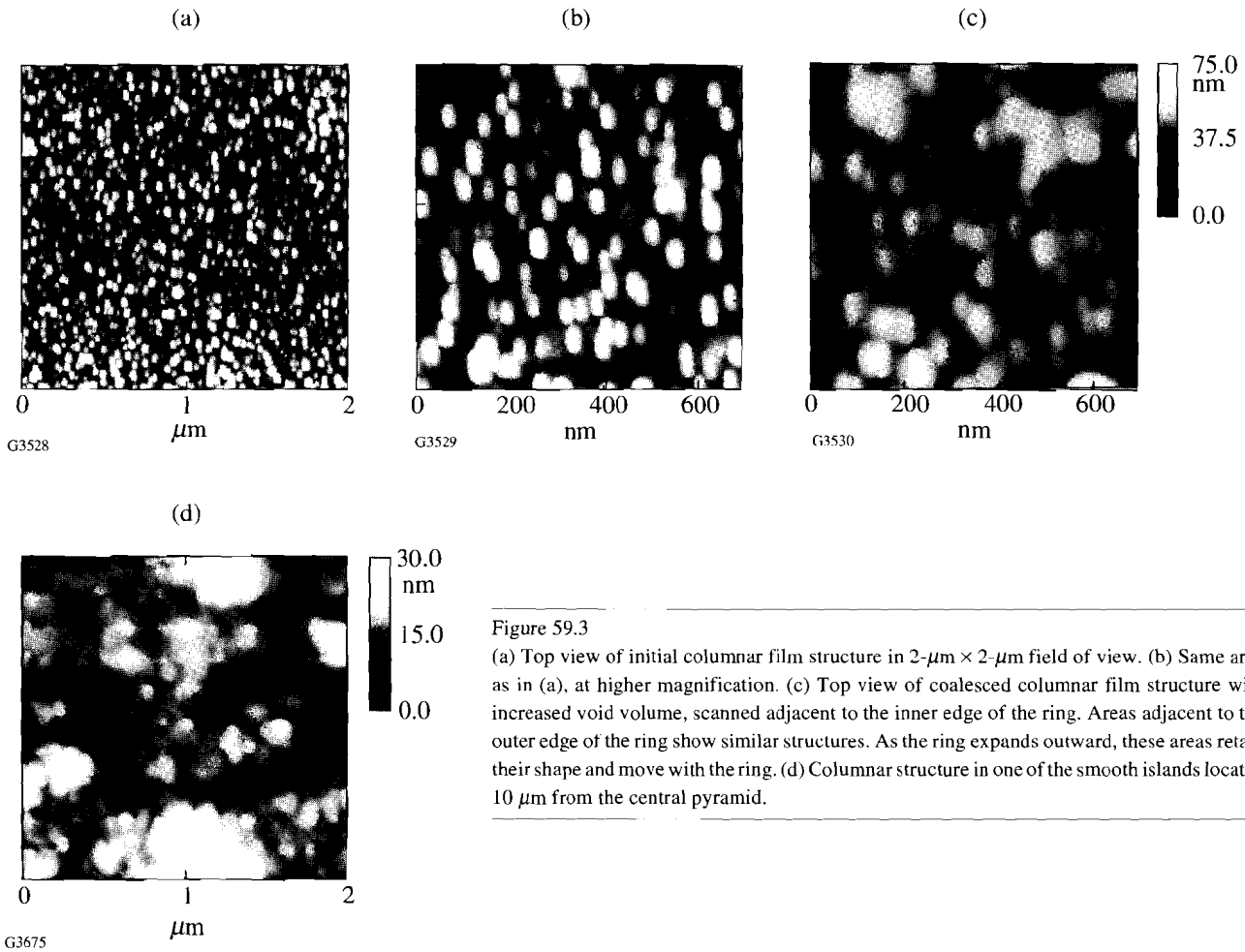

Figure 59.3
(a) Top view of initial columnar film structure in 2-μm × 2-μm field of view. (b) Same area as in (a), at higher magnification. (c) Top view of coalesced columnar film structure with increased void volume, scanned adjacent to the inner edge of the ring. Areas adjacent to the outer edge of the ring show similar structures. As the ring expands outward, these areas retain their shape and move with the ring. (d) Columnar structure in one of the smooth islands located 10 μm from the central pyramid.

islands located 10 μm from the central pyramid. Although columnar structure still exists, the columns' spatial frequencies have changed relative to the initial spatial frequencies shown in Fig. 59.3(a) at identical magnification and in Fig. 59.3(b) in a 700-nm × 700-nm "close-up" of a film area unaffected by water (the scanned, unaffected area is >1 mm away from the center of the water-penetration island). The lower spatial frequency of the columns is accompanied by a reduction in rms roughness to below 4 nm.

Figure 59.3(c) depicts a 700-nm × 700-nm top view of film columns and voids in the zone adjacent to the inner edge of the ring. Here, voids have widened because of columns that coalesced into coarser structures. The rms surface roughness remains unaffected by this coalescence [8.9 nm in the area of Fig. 59.3(c) versus 9 nm in the initial film].

The ring itself exhibits a very rough granular structure with average grain size varying between 300 and 400 nm (Fig. 59.4). The internal structure and/or porosity of these grains is yet unresolved.

The central pyramidal structures are monolithic with many, varying-size steps (1- to 100-nm scale) decorating the surfaces (Fig. 59.5). Until now, it was not possible to unambiguously determine the crystalline structure and, by implication, the solid-state phase of the yttrium-oxide complex making up the pyramids. This critical determination was hampered by signal-to-noise limits and by probe-tip geometry restrictions. The arrival of "oxide-sharp Si_3N_4" tips is expected to facilitate unraveling this important information that permits identifying the physico-chemical transport mechanism underlying the topographical patterns shown here.

Forced-Humidity Tests

When observing moisture-penetration results from a regular laboratory environment, one needs to remain aware of contaminants in the air that potentially shift the neutral water-

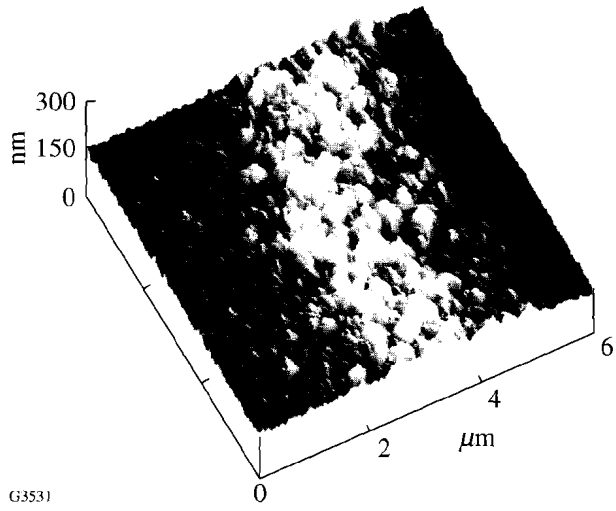

Figure 59.4
View of the 300- to 400-nm average grain size of a portion of the highly granular, well-developed ring.

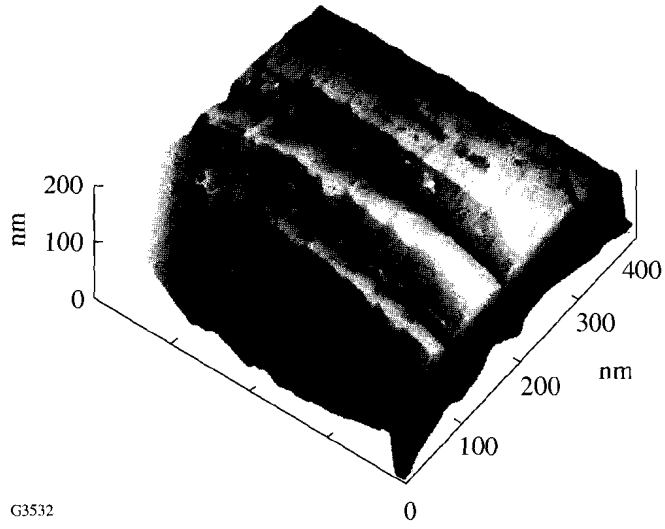

Figure 59.5
View of planar dislocation steps along the trapezoidal surface of a central pyramid. The translational regularity is indicative of the pyramid's crystallinity.

vapor pH to the basic or acidic side. In order to explore to what extent pure water drives these morphological changes, an artificial, 100%-relative-humidity condition was set up, and, independently, seeding of films by microdroplets was carried out. Samples left the humidity environment only during periods of testing. After 50 cumulative hours of exposure to 100% humidity, the first, nascent water-penetration marks became observable in a form familiar to regular laboratory effects (Fig. 59.6). This proved that water alone can promote Y_2O_3 morphological changes. The question then arose as to whether forced filling of the film pores would accelerate the mass transport such that changes driven by vapor-phase concentration over periods of months could become observable within hours or minutes.

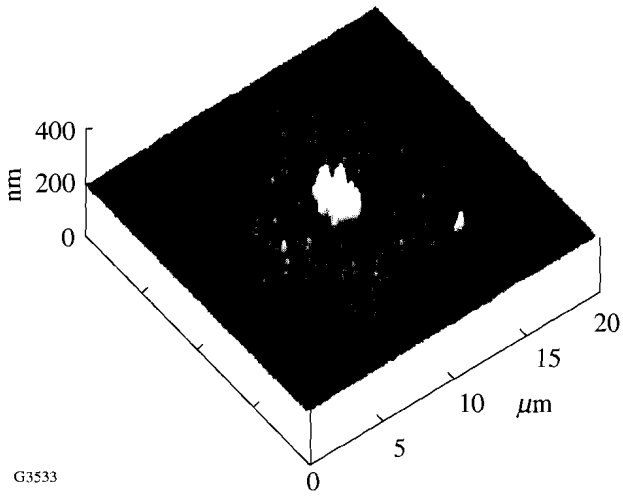

Figure 59.6
Moisture-penetration pattern in Y_2O_3 developing under 100%-relative-humidity, 50-h exposure.

After dowsing with 300-nl droplets, which each covered 0.35 to 0.60 mm^2, pyramidal pattern growth set in within 24 h [Figs. 59.7(a) and 59.7(b)] and continued for several weeks until an equilibrium pattern was established; however, ring structures failed to evolve. Instead, a high density of pyramids (of the order of 1 per 10 μm^2) was found, with film material between pyramids remaining [Fig. 59.7(c)] largely unmodified. Both the pattern-initiation sites and the transport mechanism for ring growth and expansion are therefore much likely different under vapor-phase conditions from mechanisms of fluid-phase chemistry active in forced seeding.

Conclusion

Long-term morphological changes induced by water penetration in Y_2O_3 monolayer films exhibit a pattern evolution that greatly influences atomic-force microscopy observations of such film surfaces. The finding that such films tend to uncontrollably change while one is watching them now has a rational basis. Growth patterns include distinct pyramidal features that either roughen the film during the early phase of growth kinetics or aggregate with time, leaving behind circular islands within which the typical dielectric-film, co-

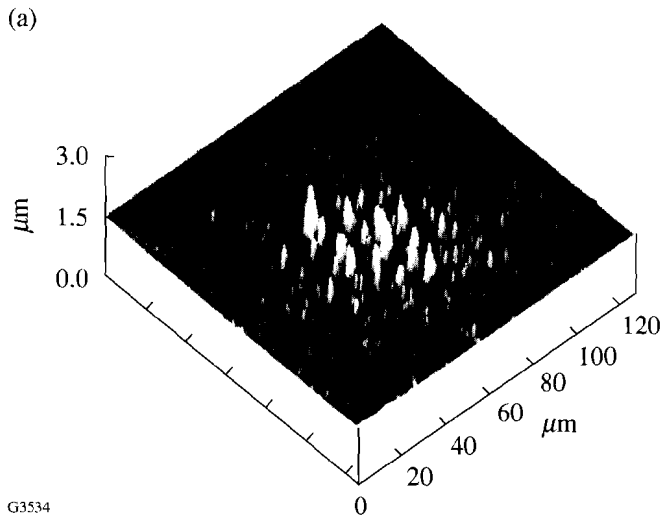

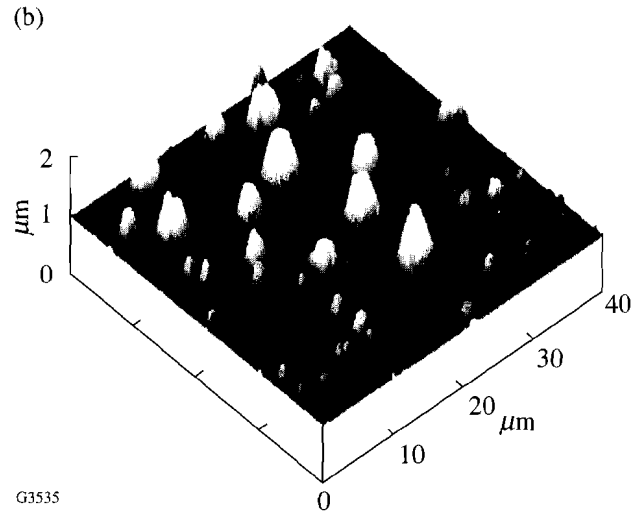

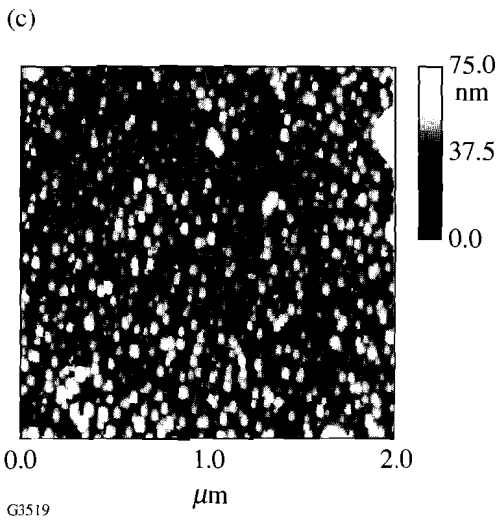

Figure 59.7
(a) Pyramidal growth pattern 24 h after seeding the site by 300-nl water droplets. (b) 40-μm × 40-μm area of (a), showing size distribution of pyramids. (c) View of a microdroplet-seeded area. The columnar spatial frequency in the area between pyramids is identical to that of the unaffected film areas, indicative of the absence of column-coalescence processes prevalent in vapor-phase-driven water penetration.

lumnar-growth structures have been irreversibly modified. The underlying mechanism for this redistribution of material is most intriguing but remains unresolved, pending further improvements in our experiment. It is already clear, however, that no additives to water are needed to promote the process. From an end-user concern, it is important to screen whether (and which, if any) additives, such as surfactants or solvents used in cleaning and maintenance of laser systems and infrastructures, further enhance film degradation through mechanisms evidenced here.

ACKNOWLEDGMENT

This work was supported by the U.S. Department of Energy Office of Inertial Confinement Fusion under Cooperative Agreement No. DE-FC03-92SF19460 and the University of Rochester. The support of DOE does not constitute an endorsement by DOE of the views expressed in this article. This work was carried out on equipment of the Center for Optics Manufacturing (COM). The COM is a DOD Center of Excellence by the U.S. Army Material Command.

REFERENCES

1. H. K. Pulker and E. Jung, Thin Solid Films **9**, 57 (1971).
2. S. Ogura and H. A. Mcleod, Thin Solid Films **34**, 371 (1976).
3. H. A. Mcleod and D. Richmond, Thin Solid Films **37**, 163 (1976).
4. N. E. Holm and O. Christensen, Thin Solid Films **67**, 239 (1980).
5. T. M. Donovan and P. A. Temple, in *Laser-Induced Damage in Optical Materials: 1979* (SPIE, Bellingham, WA, 1980), Vol. 568, pp. 237–246.
6. H. Sankur and W. Gunning, J. Appl. Phys. **66**, 807 (1989).
7. S. G. Saxe *et al.*, Appl. Opt. **23**, 3633 (1984).

Observation of Longitudinal Acceleration of Electrons Born in a High-Intensity Laser Focus

We have measured the energy and angular distributions of electrons born in and ponderomotively accelerated from a high-intensity laser focus. The angular distribution relative to the $\vec{k}$ of the laser shows the first observation of electrons ejected with momentum in the $\vec{k}$ direction. This forward acceleration comes from the conservation of momentum in the photon field.

At very-high laser intensities, a free electron's oscillatory motion in a laser field becomes anharmonic. A detailed, theoretical examination of electron trajectories and emitted harmonic radiation was conducted by Sarachik and Schappert in 1970.[1] They parameterized the nonlinear electromagnetic wave effects by q (sometimes called η),

$$q^2 = 2\frac{e^2\langle A^2\rangle}{m_0^2c^4}, \tag{1}$$

where c is the speed of light, e and m_0 are the electron charge and rest mass, respectively, ω is the laser frequency, and $\langle A^2\rangle$ is the time average of the square of the vector potential of the laser. When $q < 1$, it is related to the ponderomotive potential (average quiver energy) of the laser, by $\Phi_{\text{pond}} = q^2mc^2/4$. When q approaches 1, a significant drift of the electron in the direction of field propagation arises. This drift, first predicted quantum mechanically in 1964 by Brown and Kibble[2] and classically by Eberly and Sleeper[3] in 1968, is second order in q.

In a laser focus, even at small q, an electron feels a force along the gradient of the ponderomotive potential. At moderate intensities, an electron born in a cylindrically symmetric laser focus with $\mathbf{k}$ in the z direction, is radially accelerated out of the focus.[4,5] An electron gains the full ponderomotive energy if the laser pulse duration τ_L is longer than the time it takes the electron to escape from the laser focus, τ_{esc}. If the laser pulse duration is sufficiently long, the electron's final kinetic energy for linear polarization is equal to its initial energy plus the ponderomotive potential at which it was born.[6] For circular polarization, the electron's final energy is twice its ponderomotive potential due to the conservation of angular momentum in the laser field.[7,8] An electron that is incident on a laser focus can be scattered off the ponderomotive potential, and, in the case of the standing wave, the electron can be Bragg scattered—the Kapitza-Dirac effect.[9] These effects were observed by Bucksbaum *et al.*[10,11] These and all other ponderomotive experiments have examined first-order effects in q and have been conducted with $q << 1$.

References 1–3 assumed that a free electron was initially at rest before the interaction with a plane-wave laser field. In our experiments an electron is released via ionization into the presence of an already intense electromagnetic field. The measurement of electrons with energies exceeding the minimum required for ionization has been labeled above threshold ionization (ATI) and reviewed recently by Freeman and Bucksbaum.[12] Electrons created by ionization are typically released with a few electron volts of energy, which can be considered to be at rest when the ponderomotive potential is much larger. This was observed in experiments by Corkum *et al.*,[7] where $q \sim 0.01$ and the electrons were observed in the radial direction due to their initial drift velocity. Free-electron interactions with laser pulses where q approaches 1 are examined in this experiment. This allows examination of second-order effects in q and, in particular, the predicted longitudinal drift.

The longitudinal drift of an electron was shown by Corkum *et al.*[13] to arise from the absorbed longitudinal momentum that accompanies the energy absorption from the focused laser field. The longitudinal momentum p_z is related to the perpendicular momentum by[13]

$$p_z = \frac{p_\perp^2}{2m_0c}. \tag{2}$$

The perpendicular momentum is related to the total energy by $p_\perp = m_0c\sqrt{2(\gamma-1)}$.[13] Electrons leave the laser focus at an

angle θ with respect to the k vector of the laser given by

$$\theta = \tan^{-1}\sqrt{\frac{2}{\gamma - 1}}. \tag{3}$$

The perpendicular momentum arises from two sources: the conservation of canonical angular momentum[1,14] and the ponderomotive acceleration out of the focus.[2,3]

The longitudinal drift arising from the conservation of angular momentum can be derived from the Hamilton-Jacobi method of Sarachik and Schappert[1] or directly from the invariance of the canonical momentum and energy.[14] If the electron is assumed to be born at $t = 0$ in a field that is uniform in the transverse direction, the electron drift velocity in the nonrelativistic limit, after the laser pulse has passed, is

$$\vec{v}_D = \frac{e}{mc}\vec{A}(0) + \frac{\vec{k}}{|k|}\frac{e^2A^2(0)}{2m^2c^3}. \tag{4}$$

The first term in Eq. (4) represents the transverse drift associated with the conservation of canonical angular momentum; the second term is the associated longitudinal drift. Equation (4) agrees with Eq. (2). If the electron is assumed to be born at the peak of the field, then $A(0) = 0$ for linear polarization, while $|A(0)| = c|E(0)|/\omega$ for circular polarization, where $E(0)$ is the electric field at the time the electron is born.

Reiss[15] and Delone and Krainov[16] have performed detailed calculations of the initial momenta of electrons produced due to the ionization of atoms in strong fields. Both found that for circular polarization the electrons had a forward momentum that was consistent with Eq. (4).

A second radial drift is associated with ponderomotive acceleration out of the laser focus.[2,3] In the weakly relativistic limit, $q < 1$, the radial ponderomotive energy is given by

$$\Phi_p = \frac{e^2\langle A^2\rangle}{2mc^2} = \frac{e^2\langle E^2\rangle}{2m\omega^2}, \tag{5}$$

where $\langle A^2\rangle$ is the temporal average of the square of the vector potential at the time of ionization. Thus for weakly relativistic conditions, an electron born in the focus of a laser pulse will have a final perpendicular velocity

$$v_{\perp r}(\infty) = \left\{\frac{2}{m}\left[\left(\frac{eA(0)}{\sqrt{2}mc^2}\right)^2 + \Phi_{\text{pond}}\right]\right\}^{\frac{1}{2}}\hat{r}. \tag{6}$$

In the above analysis, it is assumed that the laser pulse duration is long enough that the electrons can turn all of the ponderomotive energy into directed kinetic energy.[6] We can combine Eq. (6) with Eqs. (2) and (4) to determine the final drift velocity for circular polarization when $\tau_{\text{esc}} << \tau_L$,

$$\vec{v}_D(\infty) = \sqrt{2}v_{\text{osc}}\hat{r} + \frac{v_{\text{osc}}^2}{c}\hat{z}, \tag{7}$$

and for linear polarization,

$$\vec{v}_D(\infty) = \frac{v_{\text{osc}}}{\sqrt{2}}\hat{r} + \frac{v_{\text{osc}}^2}{4c}\hat{z}. \tag{8}$$

The quiver velocity v_{osc} is defined in terms of the peak electric field (field at ionization),

$$v_{\text{osc}} = \frac{|eE(0)|}{m\omega}. \tag{9}$$

The drift of the electrons is shown schematically in Fig. 59.8.

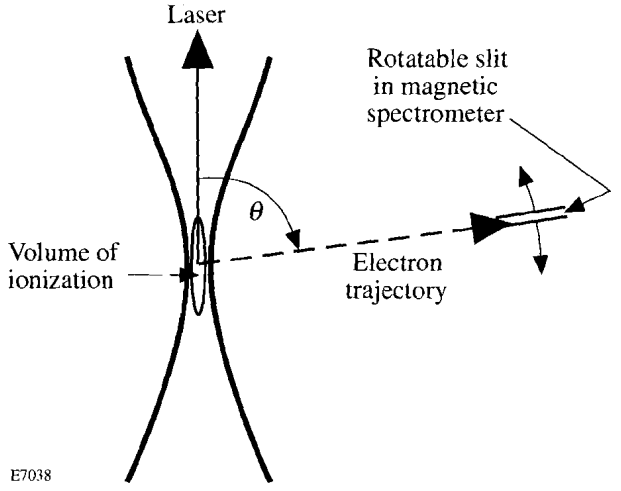

Figure 59.8
Experimental setup showing the position of the magnet gap in the spectrometer in relation to the laser focus, a typical electron trajectory, and the definition of θ. The volume of ionization refers to the volume in which the intensity exceeds the threshold intensity of ionization for a particular charge state and is not to scale.

These results have been confirmed by a fully relativistic Monte Carlo simulation of the electron dynamics. The simulation involved propagating a circularly polarized, Gaussian temporal and spatial profile laser pulse over a few thousand atoms placed at random positions within a laser focus. The laser parameters were based on measurements of the corresponding parameters of our laser system. Electrons were released into the field at the intensity necessary for Coulomb barrier suppression ionization (BSI),[17]

$$E = \frac{\varepsilon_{\text{ion}}^2}{4Z}, \tag{10}$$

where ε_{ion} is the ionization potential and Z is the ionic charge with zero initial velocity. The fully relativistic equation of motion

$$\dot{\vec{p}} = -e\vec{E} - \frac{e}{\gamma mc}\vec{p} \times \vec{B} \tag{11}$$

for the electron trajectories was solved for each electron, and the electrons' positions and velocities after exiting the focus were stored. These electron trajectories, which agreed with Eq. (7), were then convolved with the spectrometer characteristics to give the expected observed energy and angular distributions.

The experiment consisted of creating free electrons via ionization in the laser focus and measuring the ejected electron distributions as a function of energy and angle from the beam axis.

We have constructed a magnetic spectrometer to measure the energy and angular distributions of electrons emitted from a high-intensity laser focus. The spectrometer consists of a magnet for steering the electrons, a scintillator for detection of the electrons, and a photo-multiplier-tube (PMT) for detection of photons created in the scintillator.

The steering magnet is a 10-cm-square piece of high-purity iron with a 6-cm-square cut from the center. A 2-mm gap was cut in one side of the iron, and coils of wire were wrapped around the other three sides of the iron to create an electromagnet. A 100-ms square-topped pulse of voltage is applied across the coils of the magnet resulting in a magnetic field in the gap. The electromagnet is fired 80 ms before the laser pulse, allowing the magnetic field in the gap to be in a steady state by the time electrons are ionized in the laser focus. Residual fields or hysteresis effects on the iron core of the magnet are minimized by degaussing after every firing of the magnet using a slowly diminishing ac current. This technique allows magnetic fields in the gap from 50 to 6000 G to be reliably formed with less than 5% fluctuation from shot to shot.

The magnet is placed above the laser focus with the 2-mm gap aligned with the focus, allowing a line of sight to be traced from the focus through the gap in the magnet. Electrons emitted from the laser focus toward the gap in the magnet enter the gap and are curved by the magnetic field. Electrons with energies giving a gyro-radius of approximately 1.5 cm in the applied magnetic field travel through the gap and strike the scintillator where ultraviolet photons are emitted. The photon flux is then measured using the PMT, and the electrical signal is read by an analog-to-digital converter, which gives a number of counts proportional to the electron number and energy. Peak signal-to-noise ratios of 1000 to 1 are obtained with this setup. The direct line of sight from the focus to scintillator is blocked by 3 cm of aluminum shielding. Aluminum sheet metal is used elsewhere as shielding so that the only possible noise source is stray light through the gap in the magnet.

The energy window of the spectrometer is varied by changing the magnetic field in the gap of the steering magnet. A calibration has been performed using an electron gun producing electrons of known energy. The electron gun was placed at the laser focus and aimed toward the gap in the steering magnet. The magnetic field in the gap was varied by adjusting the voltage applied across the coils of the electromagnet allowing a measurement of the applied voltage versus electron energy. The calibration showed an energy window of $\Delta E/E \sim 0.3$ FWHM. Monte Carlo predictions of the calibration curve are in excellent agreement with the measured calibration.

The angular distribution of electrons in θ (relative to the k of the laser) is measured by rotating the entire spectrometer, which is cylindrically shaped. The central axis of this cylinder passes through the laser focus at 90° to the laser axis. The gap in the magnet is offset from the central axis of the spectrometer and is always aligned so that a clear line of sight can be traced from anywhere on this central axis through the gap in the magnet (see Fig. 59.8).

An angular resolution of ±2° is achieved with this setup. This uncertainty comes from two sources: The first is the geometric angular resolution due to the gap in the magnet. The gap is 2 mm wide, which corresponds to an angular spread of

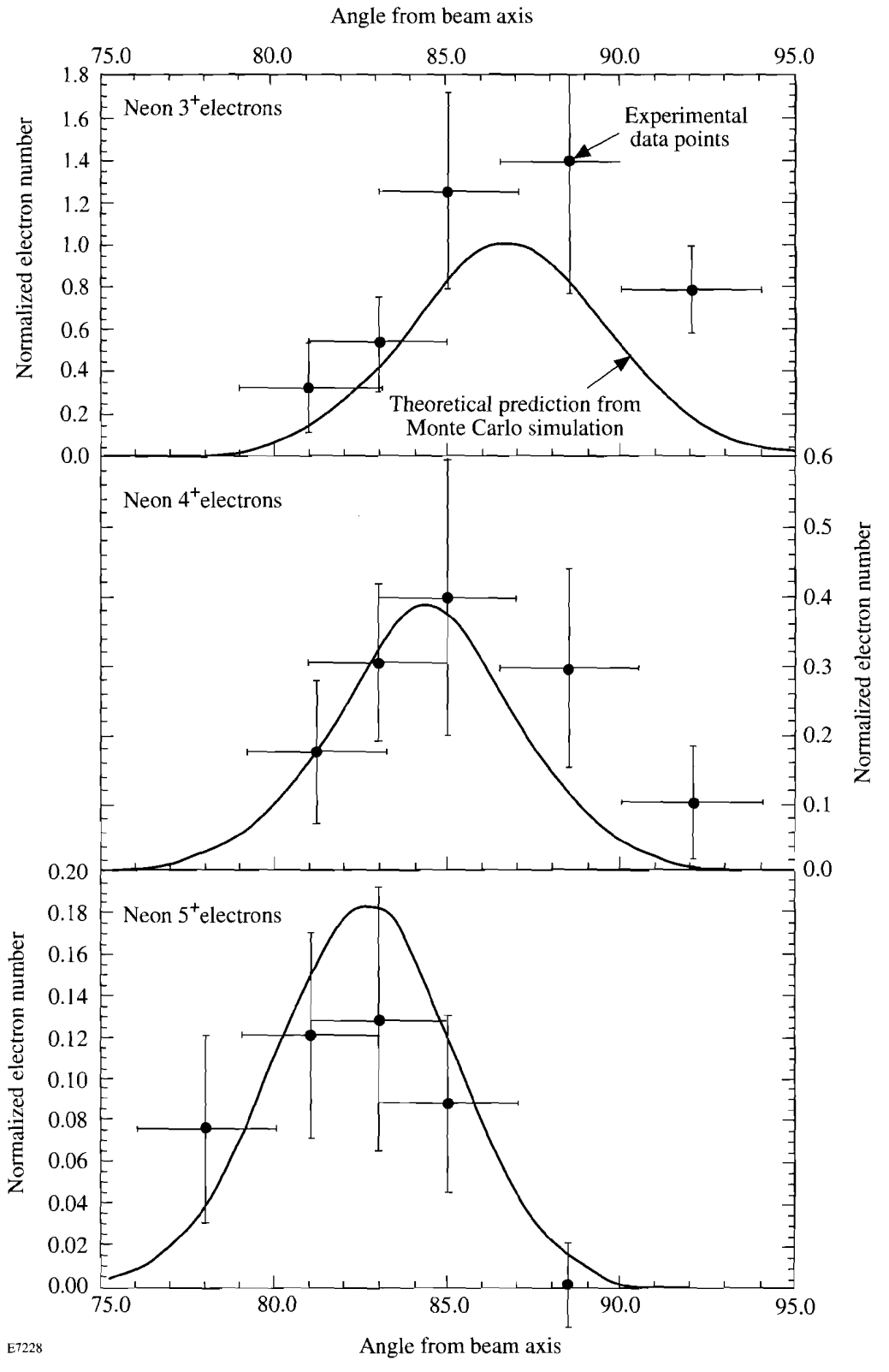

Figure 59.9
Observed experimental angular distribution data points for electrons ionized from the 3^+, 4^+, and 5^+ charge states of neon. The solid curve represents the expected angular distribution for each charge state from the theoretical Monte Carlo simulation of the electron dynamics.

±1° for electrons traveling from the laser focus. The second is due to an asymmetry in the magnetic field of the magnet in the spectrometer. A slight tilt found in the magnetic field deflected electrons by 5°±1° from their original ejection angle. This angle was determined from the detection angle of the Ne^{3+} electron peak on one side of the laser focus compared to its position on the opposite side of the focus. The symmetry of the focus requires that this peak occur at the same angle from the k vector of the laser on both sides of the focus. This was used to determine the angle of electron deflection due to the tilt in the field. This determination is accurate to ±1° and, when combined with the geometric resolving power of the gap, gives a total uncertainty in the angle of ±2°.

The experiments were performed with a 1.05-μm, 1-ps laser system using chirped-pulse amplification (CPA), which is described elsewhere.[18] The experiment discussed in this article was conducted in neon at a pressure of 5×10^{-4} Torr. The laser was focused with $f/6$ optics producing a 5-μm ($1/e^2$ radius) focal spot and a peak laser intensity of approximately 5×10^{17} W/cm^2 ($q \sim 0.5$). Circular polarization was used to avoid possible asymmetries in the electron angular distribution in the plane of polarization upon ionization due to non-zero initial velocities of the electrons along the electric field.[7]

Helium was ionized to confirm the expected ponderomotive energies associated with the BSI threshold intensities. This was accomplished by measuring the energy spectrum of helium and assuming that the highest energy electron peak was from He^{2+}. The energy of this peak was 3.0 kV, which is in agreement with the approximate expected value of 3.5 kV based on BSI in circular polarization and subsequent acceleration of the electron by the ponderomotive potential. Ne^{3+} is created at approximately the same intensity as He^{2+},[17] which was used to determine the electron peaks in the neon spectrum. Energies of the electrons ionized from the 3^+, 4^+, 5^+, and 6^+ charge states of neon were in agreement with the expected ponderomotive energies associated with their corresponding BSI threshold intensities.

Figure 59.9 shows the measured data values of the angular distribution of the 3^+, 4^+, and 5^+ electrons of neon and their expected theoretical positions based on the Monte Carlo simulation. The angular spread in the electron distributions is due primarily to the intensity distribution of the laser focus. The ponderomotive force is linearly related to the gradient of the intensity distribution, which is not always perpendicular to the beam axis in a focused Gaussian beam. As a result some electrons have a small component of ponderomotive acceleration along the beam axis. This acceleration is symmetric about 90° to the beam axis due to the symmetry of a Gaussian beam as it passes through focus and cannot explain any forward shift of the peak of the electron distribution. A normalized electron number is used on the y axis since we do not have an absolute calibration of the number of electrons striking the scintillator in the experiment. A single normalization constant was used in a least-squares fit between the Monte Carlo simulation and experimental data for all three charge states.

Figure 59.10 shows the angle of peak electron number for the 3^+, 4^+, and 5^+ neon charge states measured as a function of electron energy. The points found from the Monte Carlo simulation are in good agreement with the angular distribution predicted in Eq. (3). The experimental points are in good agreement with both of these predicted values. From this we conclude that a nonsymmetric forward acceleration of the electrons has been observed, consistent with the forward drift found in Refs. 1–3.

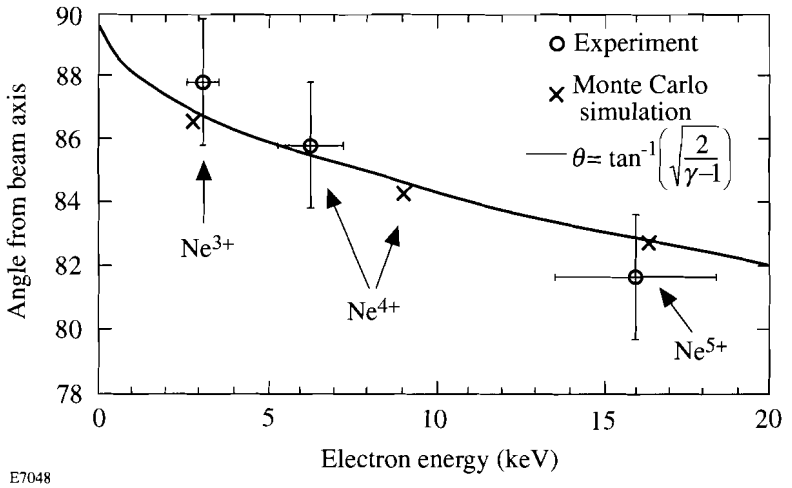

Figure 59.10
Angle of peak electron number for the 3^+, 4^+, and 5^+ electrons of neon from the theoretical Monte Carlo simulation of the electron dynamics and the observed experimental data points. The solid curve is the theoretical prediction of Eq. (4).

We have made the first observations of a forward acceleration of electrons in a high-intensity laser focus. Good agreement is shown between the forward shifted angle of the fully relativistic theoretical predictions and the data obtained.

ACKNOWLEDGMENT

The author's gratefully acknowledge conversations with J. H. Eberly. This work was supported by the U.S. Department of Energy Office of Basic Energy Sciences, Division of Chemical Sciences. Additional support was provided by the U.S. Department of Energy Office of Inertial Confinement Fusion under Cooperative Agreement No. DE-FC03-92SF19460, the University of Rochester, and the New York State Energy Research and Development Authority. The support of DOE does not constitute an endorsement by DOE of the views expressed in this article.

REFERENCES

1. E. S. Sarachik and G. T. Schappert, Phys. Rev. D **1**, 2738 (1970).
2. L. S. Brown and T. W. B. Kibble, Phys. Rev. **133**, A705 (1964).
3. J. H. Eberly and A. Sleeper, Phys. Rev. **176**, 1570 (1968).
4. H. A. H. Boot, S. A. Self, and R. B. R-Shersby-Harvie, J. Elect. Control **4**, 434 (1958).
5. T. W. B. Kibble, Phys. Rev. **150**, 1060 (1966).
6. R. R. Freeman *et al.*, Phys. Rev. Lett. **59**, 1092 (1987).
7. P. B. Corkum, N. H. Burnett, and F. Brunel, Phys. Rev. Lett. **62**, 1259 (1989).
8. P. H. Bucksbaum *et al.*, Phys. Rev. A **41**, 4119 (1990).
9. P. L. Kapitza and P. A. M. Dirac, Proc. Cambridge Philos. Soc. **29**, 297 (1933).
10. P. H. Bucksbaum, M. Bashkansky, and T. J. McIlrath, Phys. Rev. Lett. **58**, 349 (1987).
11. P. H. Bucksbaum, D. W. Schumacher, and M. Bashkansky, Phys. Rev. Lett. **61**, 1182 (1988).
12. R. R. Freeman and P. H. Bucksbaum, J. Phys. B: At. Mol. Opt. Phys. **24**, 325 (1991).
13. P. B. Corkum, N. H. Burnett, and F. Brunel, in *Atoms in Intense Fields*, edited by M. Gavrila (Academic Press, New York, 1992), pp. 109–137.
14. W. B. Mori and T. Katsouleas, Phys. Rev. Lett. **69**, 3495 (1992).
15. H. R. Reiss, J. Opt. Soc. Am. B **7**, 574 (1990).
16. N. B. Delone and V. P. Krainov, J. Opt. Soc. Am. B **8**, 1207 (1991).
17. S. Augst, D. Strickland, D. D. Meyerhofer, S. L. Chin, and J. H. Eberly, Phys. Rev. Lett. **63**, 2212 (1989).
18. Y.-H. Chuang, D. D. Meyerhofer, S. Augst, H. Chen, J. Peatross, and S. Uchida, J. Opt. Soc. Am. B **8**, 1226 (1991).

Spatial Intensity Nonuniformities of an OMEGA Beam due to Nonlinear Beam Propagation

Several applications require that a laser beam maintain a high degree of wavefront quality after propagating a long distance through air. In particular, laser drivers for inertial confinement fusion use intense laser beams that propagate tens of meters through air to a fusion target. Many amplification stages are required in the system to reach the energy levels required for each beam. Good beam quality is essential throughout the system to prevent the onset of nonlinear effects that can lead to optical damage or wavefront degradation. To maintain beam quality, spatial filters are used between amplification stages to remove high-spatial-frequency modulation impressed onto the beams by random or fixed phase distortions in the beam paths. Despite the use of spatial filters, the wavefront quality of a high-energy laser can be degraded, and nonlinear optical effects can occur in the system.

Forward stimulated rotational Raman scattering (SRRS) can be generated when intense laser fields propagate through air[1–3] due to the N_2 molecules in the interaction path. This unwanted Raman radiation can degrade the spatial as well as the temporal characteristics of the beam. In addition, when a high-energy laser is focused into a spatial filter, the residual material remaining in the spatial filter can act as a nonlinear medium to again degrade the beam quality.

It is well known that for Raman scattering the coupling between the Raman Stokes and anti-Stokes radiation in a dispersive medium leads to the generation of conical emission.[4] The Stokes and anti-Stokes radiation is emitted at angles to the optical axis due to phase matching and is azimuthally symmetric about the optical axis. If the cylindrical symmetry of the pump wave is broken, then another phase-matched four-wave-mixing process can break the azimuthal symmetry of the conical emission, and a transverse modulational instability can occur. This instability manifests itself as preferential gain at six angles uniformly spaced around the cone, resulting in six intensity peaks around the cone resembling a hexagonal intensity distribution in the far field. Evidence of this four-wave-mixing convective instability was first reported by Tan-No *et al.*[5] in 1980. Since then several other observations have been reported along with several theoretical analyses.[5–13] The majority of the work in this field has been performed with counter-propagating pump beams in a nonlinear medium. A notable exception is the work of Pender and Hesselink,[9] who observed this instability with a single forward pump wave as in the experiments performed with the OMEGA laser to be discussed here.

Two separate experiments were performed with the OMEGA laser that show evidence of this transverse modulational instability. In the first experiment a beam underwent free propagation through air, and the instability was observed in the presence of SRRS. In the second experiment a 1-kJ laser was focused into a vacuum spatial filter having a 50-μm residual fill pressure, and the instability was observed in the near field after the spatial filter. These experiments illustrate that in order to determine the details of the spatial structure of an intense beam propagating in a nonlinear medium, this four-wave-mixing transverse modulational instability must be considered.

Experiments

Two separate experiments that exhibit transverse modulational instabilities were performed. In one experiment, the generation of SRRS in air was studied to determine the effects of SRRS on the propagation of OMEGA Upgrade beams as they propagate through air to a target. In another experiment the requirements on the final fill pressure for high-energy spatial filters was studied.

In the first experiment[2] a third-harmonic beam at 351-nm wavelength 600-ps full-width at half-maximum (FWHM) from the OMEGA laser was down collimated to approximately a 5-cm beam diameter and propagated over a 35-m path length in air. The near-field beam intensity profile was recorded on film at the beginning and end of the beam path. The spectral content of the beam was also recorded on film at the end of the air path using a 1-m spectrometer. The film was

developed, digitized with a microdensitometer, and converted to intensity exposure by using the appropriate film-density, log-intensity calibration for the film and for the experimental conditions used.

The spectrum, displayed in Fig. 59.11, clearly shows the generation of Stokes and anti-Stokes radiation from the SRRS process in air. For this experiment approximately 1% of the laser energy was converted to SRRS.

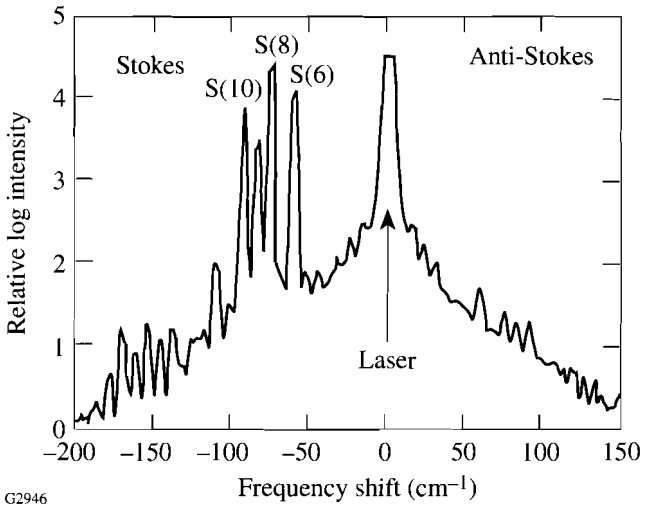

Figure 59.11
Raman spectrum showing several of the *S* transitions of nitrogen in air. The pump laser saturated the film at a frequency shift equal to zero.

The intensity distribution at the end of the 35-m air path is shown on a log scale in Fig. 59.12, where strong intensity modulation can be seen. To determine the spatial frequency content of the beam at the end of the air path, a two-dimensional FFT was calculated from the measured intensity distribution. To highlight the features in the FFT, the central portion of the FFT (containing the near dc spatial components) was blocked, and the FFT was plotted on a log scale, as shown in Fig. 59.13. Although the FFT is symmetric about positive and negative frequencies, it clearly shows evidence of the hexagonal pattern in the far field associated with the transverse modulational instability.

In the second experiment a beam with 1 kJ of energy, 700-ps FWHM, and a 1054-nm wavelength was focused into a spatial filter. The spatial filter input and output beam diameters were 18 cm, and the *f* number of the spatial filter was equal to 14. In an attempt to determine the maximum fill pressure allowed for this spatial filter with these beam param-

Figure 59.12
Near-field intensity distribution of the beam after propagating 35 m in air, plotted on a log scale.

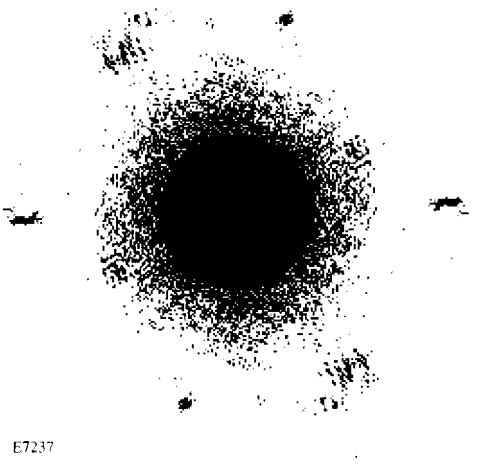

Figure 59.13
FFT of the near-field intensity distribution of the beam after propagating 35 m in air. The central portion of the FFT containing the low spatial frequencies was blocked, and the remaining FFT was plotted on a log scale. The hexagonal intensity distribution surrounding the central spot can be seen and is caused by the transverse modulational instability.

eters, the fill pressure was varied, and the beam intensity distribution after the spatial filter was recorded on film. The film was again digitized and intensity converted. The input beam to the spatial filter was slightly astigmatic. The intensity modulation on the beam exiting the spatial filter with a 50-μm residual fill pressure (the highest pressure used in the experiments) is shown in Fig. 59.14. To enhance the intensity modulational features on the image of the beam, a constant intensity (equal to 80% of the maximum intensity) was subtracted from the digitized near-field intensity distribution of the beam. The results are shown in Fig. 59.14. In this figure a hexagonal intensity distribution can be seen at the approximate center of the distribution centered on the cross with a diameter approximately equal to the beam radius. Additional modulation at the edges of the intensity distribution can also be seen. For this experiment, no measurements were made of the spectral content of the beam.

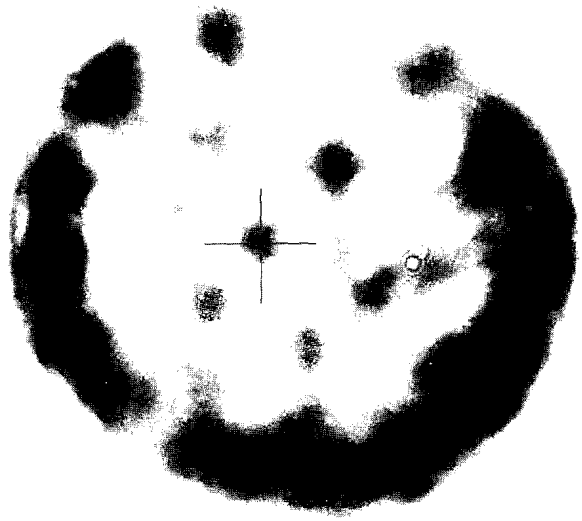

E7238

Figure 59.14
Near-field intensity distribution of a 1-kJ beam at 1054-nm wavelength after propagating through a spatial filter with a 50-μm residual fill pressure. To help illustrate the modulation, 80% of the beam intensity was subtracted from the image. The hexagonal intensity distribution caused by the transverse modulational instability can be seen centered on the cross with a diameter approximately equal to the beam radius.

The above experiments show evidence of a transverse modulational instability with a high-energy laser. The observed hexagonal intensity distributions are characteristic of a four-wave-mixing interaction that can be understood through simple modeling using the plane-wave approximation.

Theory and Discussion

Stokes and anti-Stokes SRRS will be generated when an intense laser beam propagates over a long path in air. Appreciable amounts of this radiation are created when the product of the laser intensity times the interaction length exceeds a minimum threshold. In a dispersive medium, the coupling between the Stokes and anti-Stokes fields leads to conical emission. If the pump laser is not cylindrically symmetric, then the coupling between the Stokes and anti-Stokes fields can lead to the observed transverse modulational instability.

To see the origin of this transverse modulational instability we follow the analysis of Pender and Hesselink[9] and begin with the wave equation in a Raman active medium:

$$\nabla^2 E - \frac{n^2}{c^2}\frac{\partial^2 E}{\partial t^2} = \frac{4\pi}{c^2}\frac{\partial^2 P^{NL}}{\partial t^2}, \tag{1}$$

where the nonlinear polarization is given by

$$P^{NL} = \chi^{(3)} E^3 . \tag{2}$$

We assume that the seven waves making up the hexagonal intensity distribution (the six waves uniformly spaced around the cone plus one on axis) are all linearly polarized, have the same frequency (such as all Stokes frequencies), and propagate in the near forward direction (i.e., no counterpropagating beams). For clarity the seven waves are shown in Fig. 59.15. In the plane wave approximation we assume that the total electric field E is given by the sum of the laser field and a sum over seven Stokes and seven anti-Stokes fields. With these assumptions, the total electric field in the medium is given by

$$E = E_L e^{-i(\omega_L t + \mathbf{k}_L \cdot \mathbf{z})} + \sum_{j=0}^{6} E_{Sj} e^{-i(\omega_S t + \mathbf{k}_{Sj} \cdot \mathbf{z})} + \sum_{j=0}^{6} E_{Aj} e^{-i(\omega_A t + \mathbf{k}_{Aj} \cdot \mathbf{z})} + cc, \tag{3}$$

where the subscripted E's are the amplitudes of waves with frequency ω and wave vector $\mathbf{k}$, and the subscripts L, S, and A denote the laser, Stokes, and anti-Stokes fields, respectively. If we cube this total electric field, substitute into the optical wave Eq. (1) with the appropriate nonlinear polarization [Eq. (2)], and make the standard assumptions in steady state, we get for a typical Stokes field ($S1$ in Fig. 59.15, for example)

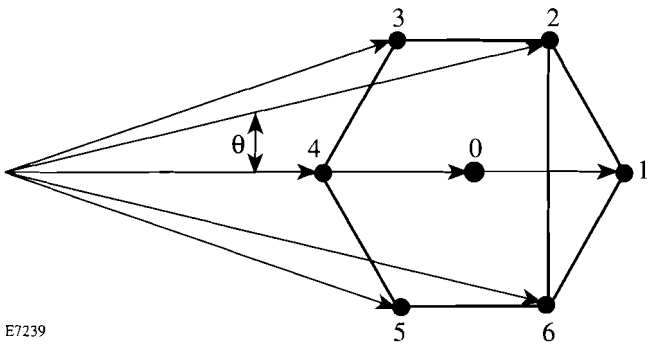

Figure 59.15
Diagram of the seven beams making up the hexagonal intensity distribution characteristic of the transverse modulational instability.

$$\frac{\partial E_{S1}}{\partial z} = -i\gamma\left\{|E_L|^2 + \sum_{j=0}^{6}|E_{Aj}|^2 + \sum_{j=0}^{6}|E_{Sj}|^2 - \frac{1}{2}|E_{S1}|^2\right\}E_{S1}$$

$$-i\frac{\gamma}{2}E_L^2E_{A4}^*\exp[-i\Delta k_{A4}z]$$

$$-i\frac{\gamma}{2}E_{S0}^*E_{S2}E_{S6}\exp[+i\Delta kz]$$

$$-i\frac{\gamma}{2}E_{S0}\left(E_{S2}E_{S3}^* + E_{S6}E_{S5}^*\right)\exp[-i\Delta kz]$$

$$-i\frac{\gamma}{2}E_{S4}^*E_{S0}^2\exp[-i2\Delta kz]$$

$$-i\frac{\gamma}{2}E_{S4}^*\left(E_{S2}E_{S5} + E_{S3}E_{S6}\right) \qquad (4)$$

with $\Delta k_{Aj} = \left(2\mathbf{k}_L - \mathbf{k}_{S1} - \mathbf{k}_{Aj}\right)\cdot\mathbf{z}$ and $\Delta k = k(1-\cos\theta)$ and where θ is the cone angle for Stokes and anti-Stokes coupling and γ is the coupling coefficient. This equation describes the evolution of one of the Stokes waves (wave $S1$) in the medium and has many contributions that will be discussed further to provide insight into the nature of the instability.

The first term on the right in Eq. (4) contains the intensity-induced refractive index terms and gives rise to ordinary stimulated scattering. The second term on the right is the Raman Stokes and anti-Stokes coupling term that can be completely phased matched $\left(\Delta k_{Aj} = 0\right)$, even in a dispersive medium. In a dispersive medium phase matching occurs when the Stokes and anti-Stokes fields propagate at some angle to the optical axis giving rise to conical emission. (This second term has azimuthal symmetry and is present for any choice of Stokes wave around the cone.)

The third and fourth terms are largely responsible for the transverse modulational instability. The third term on the right is a near-phase-matched, four-wave-mixing term and gives rise to loss for $S1$, i.e., one photon is absorbed from each of beams $S0$ and $S1$ and reemitted into beams $S2$ and $S6$. Near complete phase matching for this process occurs and can be seen from Fig. 59.15 since a line drawn through $S2$ and $S6$ and a line drawn through $S0$ and $S1$ bisect one another. (A small phase mismatch Δkz exists due to the off-axis propagation of the waves involved. Perfect phase matching would occur only for all waves propagating in the forward direction; however, the additional gain provided in this off-axis direction by ordinary conical emission outweighs the loss due to this phase mismatch.) In a similar manner, the fourth term on the right contains two near-phase-matched (by the same argument given for the third term), four-wave-mixing terms. These contributions give rise to additional gain for $S1$ at the expense of the pair of waves $S2$ and $S3$ and the pair $S5$ and $S6$. Hence, hexagonal position $S1$ has two gain contributions [Eq. (4), term (4)] and one loss contribution [Eq. (4), term (3)] resulting in net gain due to the four-wave-mixing process associated with the transverse modulational instability. This implies that if Stokes wave $S1$ is present, it will lead to the efficient generation of the other Stokes waves around the hexagon since we can rotate the cone by 60° and repeat the argument. The location of $S1$ along the cone, however, is arbitrary, and for an azimuthally symmetric pump laser we would expect ordinary conical emission. If, on the other hand, the pump laser is not perfectly symmetric about the optic axis, then the Stokes wave at $S1$ may experience higher gain than the other waves around the cone, which will initiate the instability leading to the formation of the hexagonal intensity distribution.

The fifth and sixth terms on the right are terms that contribute to uniform gain around the cone and, hence, do not contribute to the instability.

Equation (4) was derived assuming that only seven Stokes waves were present. For analytical purposes Pender and Hesselink assumed 13 waves in their analysis (12 waves uniformly spaced around the cone plus one on axis). In their numerical analysis they show that for uniform seeding of all 13 waves only ordinary conical emission results. If, on the other hand, one of the waves on the cone is seeded with a

higher intensity then the others, this wave and the other five waves making up the corresponding hexagonal intensity distribution see higher gain than the remaining six around the cone. In fact, the six waves that do not see gain actually experience loss, implying that, in this case, energy is redistributed around the cone favoring the hexagonal pattern formation. Equation (4) is in the same form as that of Pender and Hesselink, and, hence, their results are expected to apply here. Thus, it is plausible to expect a transverse modulational instability to occur in the presence of stimulated Raman scattering as was observed in the experiments discussed above.

Conclusions

Transverse modulational instabilities have been observed in an OMEGA beam in two separate experiments. In one experiment a collimated beam with 351-nm wavelength propagated through air, and the instability was observed in the presence of stimulated rotational Raman scattering. In the second experiment, the instability was observed when a 1-kJ laser pulse with 1054-nm wavelength was focused into a spatial filter having a 50-μm residual pressure. In both experiments, the transverse modulational instability took the form of a hexagonal intensity distribution in the far field of the interaction region.

A qualitative analysis of the instability can be performed in the plane-wave approximation. The instability is due to a phase-matched, four-wave-mixing interaction involving the Raman Stokes and anti-Stokes fields in the medium. The data and analysis agree well with similar work in the field. A complete analysis of the beam intensity modulation on a high-energy laser should include the effects of this transverse modulational instability.

ACKNOWLEDGMENT

The author thanks J. Kelly, K. Thorp, and M. Tedrow for experimental results that lead to Fig. 59.14 and to R. Bahr for his work on the SRRS experiment. This work was supported by the U.S. Department of Energy Office of Inertial Confinement Fusion under Cooperative Agreement No. DE-FC03-92SF19460, the University of Rochester, and the New York State Energy Research and Development Authority. The support of DOE does not constitute an endorsement by DOE of the views expressed in this article.

REFERENCES

1. M. A. Henesian, C. D. Swift, and J. R. Murray, Opt. Lett. **10**, 565 (1985).
2. M. D. Skeldon and R. E. Bahr, Opt. Lett. **16**, 366 (1991).
3. Laboratory for Laser Energetics LLE Review **52**, NTIS document No. DOE/DP/40200-229, 1992 (unpublished), p. 211.
4. N. Bloembergen, *Nonlinear Optics* (The Benjamin/Cummings Publishing Co., Inc., MA, 1982).
5. N. Tan-No, T. Hoshimiya, and H. Inaba, IEEE J. Quantum Electron. **16**, 147 (1980).
6. G. Grynberg, Opt. Commun. **66**, 321 (1988).
7. G. Grynberg *et al.*, Opt. Commun. **67**, 363 (1988).
8. A. L. Gaeta, M. D. Skeldon, R. W. Boyd, and P. Narum, J. Opt. Soc. Am. B **6**, 1709 (1989).
9. J. Pender and L. Hesselink, J. Opt. Soc. Am. B **7**, 1361 (1990).
10. R. Chang *et al.*, Opt. Commun. **88**, 167 (1992).
11. J. B. Geddes, J. V. Moloney, and R. Indik, Opt. Commun. **90**, 117 (1992).
12. J. Y. Courtois and G. Grynberg, Opt. Commun. **87**, 186 (1992).
13. M. Tamburrini *et al.*, Opt. Lett. **18**, 855 (1993).

Calculated X-Ray Backlighting Images of Mixed Imploded Targets

Shell-core mixing, which can occur during the deceleration phase of a laser-driven implosion, is believed to be the major limitation on target performance. This mixing is brought about by a hydrodynamic instability during the deceleration phase, which is seeded by instability generated during the acceleration phase due to laser and target nonuniformities.[1] The image of the x-ray emission from the shell (enhanced by high-Z doping) was used in recent experiments to diagnose this effect.[2] Because of the limb effect, this emission appears in the image in the form of a ring; mixing causes this emission ring to move toward smaller radii. However, the difference in the image characteristics between mixed targets and unmixed targets, which compress to a smaller radius, is subtle: in the former case, the outward drop in intensity is slower. Thus, a smaller compression and mixing tend to cancel each other's effect on the position of the ring in the image.

We show here that when backlighting imaging is used in the experiment, that uncertainty can be largely removed. An important ingredient of such imaging is the ability to record simultaneously the backlighting image as well as the image due to the target self-emission. We showed earlier[3,4] that to achieve this requirement, the image has to be monochromatized by a diffracting crystal because self-emission from predicted OMEGA Upgrade targets was shown to completely overwhelm the intensity of any backlighting radiation. However, if most of the backlighter radiation is comprised in a single spectral line to which the monochromator is tuned, the two image components can be made to have comparable intensities.

An absorption ring appears in the image, outside the ring due to target self-emission, when the proper backlighter conditions are chosen. The results of this work show that, whereas the emission ring indeed moves to smaller radii when mixing is introduced, the backlighting absorption ring is virtually unaffected. Thus, the relative position of the two rings constitutes a mixing signature. In other words, the absorption ring delineates the colder part of the shell and is a true signature of the compression, whereas the emission ring reflects the shell material motion due to mixing.

We calculate here the combined backlighting and self-emission image of a particular simulated target implosion on the OMEGA Upgrade laser. For this test case, *LILAC* results were used for the expected temperature and density profiles of the unmixed target. A post-processor code was developed[4] to calculate the transport of backlight radiation through the target, as well as the self-emission of the target itself (and its transport). A simplified procedure is used to simulate the mixing, and the radiation transport equation is then solved for the unmixed as well as the mixed targets. The total calculated image has two components that are measured simultaneously: the one due to the backlighting, and the other due to target self-emission. The former is calculated assuming a certain incident flux level, based on experiments; the latter is directly calculated from the *LILAC* profiles, using the radiation transport code developed here.

The target is a polymer shell of 940-μm diameter and 30-μm thickness, filled with 80 atm DT gas, and imploded by a trapezoidal pulse. The pulse rises linearly over a 0.1-ns period to 13.5 TW, then remains constant for 2.2 ns, before dropping linearly over a 0.1-ns period. Figure 59.16 shows the density and electron-temperature profiles predicted for this target at peak compression. The shell material has been compressed to a mean radius of ~50 μm and thickness of ~30 μm, with a density in the range of ~10 to 50 g/cm^3, corresponding to a $\rho\Delta r$ value of ~90 mg/cm^2. The electron temperature in the shell ranges from ~80 to ~800 eV. Most of the backlight radiation absorption will occur within the colder, outer part of this compressed shell.

Modeling of Target Mixing

We follow a procedure suggested by Landen *et al.*[2] for choosing the size of the spatial region over which mixing occurs during the deceleration (or burn) phase of the implosion. It is implicitly assumed that the instability during the acceleration phase is not severe enough to disrupt the shell, but it only seeds the instability due to the deceleration. Figure 59.17 describes the procedure. The $R_i(t)$ curve represents the motion of the fuel-shell interface. The free-fall line $R_{ff}(t)$ is a constant-velocity trajectory tangent to the $R_i(t)$ curve

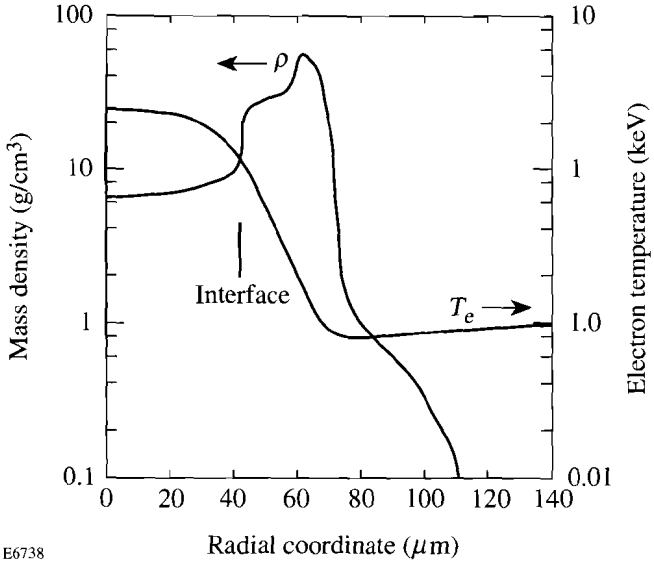

Figure 59.16
The density and electron-temperature profiles predicted by the *LILAC* code at peak compression for the case studied in this article.

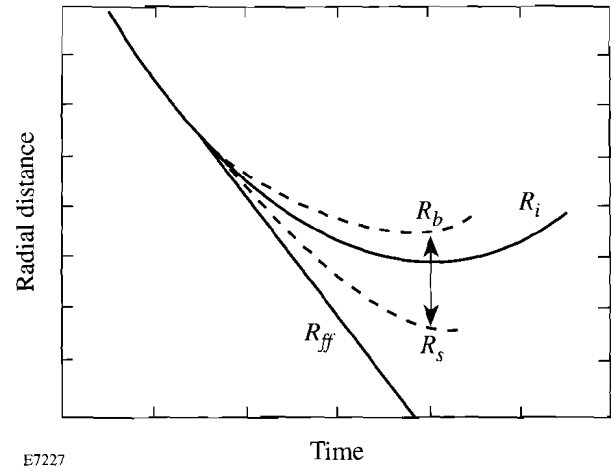

Figure 59.17
Schematic description of trajectories defining the mixed region [according to Eq. (1)]. R_i is the shell-fuel interface, R_{ff} the free-fall line, R_s the edge of the spikes region, and R_b the edge of the bubbles region. The mixed region extends from R_s to R_b.

at a time when the implosion velocity is maximal. A mixed region of F% means that the deepest penetration of shell material into the fuel region spans F% of the distance between the $R_i(t)$ curve and the free-fall line. Comparison with implosion experiments[2] on NOVA yielded a value of F ~20%; we show here results of calculations using this value and higher degrees of mixing. Simulations of Rayleigh-Taylor unstable implosions[5] show that in the nonlinear regime of the instability the shell (the heavier fluid) penetrates into the fuel (the lighter fluid) in the form of spikes. In between the spikes the fuel penetrates into the shell region in the form of bubbles whose penetration span is typically half that of the penetration of the spikes. We refer to the region comprised between $R_s(t)$ and $R_b(t)$ as the mixed region. In Fig. 59.17 the curves delineating the extreme positions of the spikes $R_s(t)$ and the bubbles $R_b(t)$ are shown schematically. Theory shows that for Atwood number 1 the amplitude of the spikes (measured from the unperturbed interface position) is twice that of the bubbles.[6] More specifically, for $F = 0.2$ the trajectories $R_s(t)$ and $R_b(t)$ will be given by

$$R_i(t) - R_s(t) = 0.2\left[R_i(t) - R_{ff}(t)\right],$$
$$R_b(t) - R_i(t) = 0.1\left[R_i(t) - R_{ff}(t)\right]. \quad (1)$$

The $R_i(t)$ curve for the test case analyzed here was plotted, and the parameters of the mixed region [$R_s(t)$ and $R_b(t)$] were determined as a function of time. At peak compression, the interface position with no mixing was $R_i = 42.7\ \mu$m, whereas the parameters of the mixed region for two particular values of F were

$$\text{for } F = 0.2: \quad R_s = 34.5\,\mu m, \quad R_b = 45.5\,\mu m$$
$$\text{for } F = 0.4: \quad R_s = 26.6\,\mu m, \quad R_b = 50.0\,\mu m. \quad (2)$$

Once the mixed region boundaries are thus determined, the procedure for the actual mixing must be determined. The manner in which the material is assumed mixed within the mixed region is somewhat arbitrary. We choose a simple prescription where the mixing is not uniform but rather decays with distance. The choice is made separately for the density of carbon ions (hence the density of shell material) and for the density of fuel ions. Using these choices, other parameters are calculated: the fraction of carbon ions out of the total ion density, the average charge $\langle z \rangle$, the total electron density, and the temperature. Figure 59.18 shows the mixing choices for the shell material and fuel (and some resulting distributions) for the test case, at peak compression (2.9 ns). Figure 59.18(a) shows the density N_C of carbon ions (atomic absorption calculations are done for C and H separately). The unmixed density curve is taken from *LILAC* runs, such as in Fig. 59.16. The

mixed curve for N_C is assumed to start from zero at R_s and to extend linearly with distance up to R_b. The slope of the curve is determined by the requirement that the mixing conserves mass (or the number of ions). As seen, this results in a jump at the $r = R_b$ position. This is not surprising if we note that the mixed profiles, such as the $N_C(R)$ curve in Fig. 59.18(a), represent lateral averages over the varying spike-bubble structure of the unstable region. The smearing, implicit in our assumption that the curves depend only on r, results in a sharp drop in laterally averaged density when crossing from the unmixed to the bubbles region.

Figure 59.18(b) shows the choice for the mixed profile of the fuel, N_F, using a slightly different prescription than that applied to the shell; N_F stands for the total density of D and T ions. The mixed curve is assumed to start from 0 at $r = R_b$ and to extend linearly inward up to the point where it meets the unmixed curve. Again, the slope of the curve is determined by the requirement that the mixing conserves mass. Because of the spike in the unmixed fuel profile near the interface, extending the linear profile all the way to $r = R_s$ would cause a transfer of fuel material from the spike inward, not only outward. Because of the choice made here, part of the fuel in the mixed region remains unaffected by the mixing (the fuel comprised between $r = 26.6$ and $r = 36.0$ μm).

To check how reasonable the resulting profiles are, we calculate the carbon fraction, defined as

$$f_C = N_C/(N_F + N_C + N_H). \quad (3)$$

Figure 59.18(c) shows that f_C is reasonably smooth and indeed reaches the correct boundary conditions: 0.5 at $r = R_b$

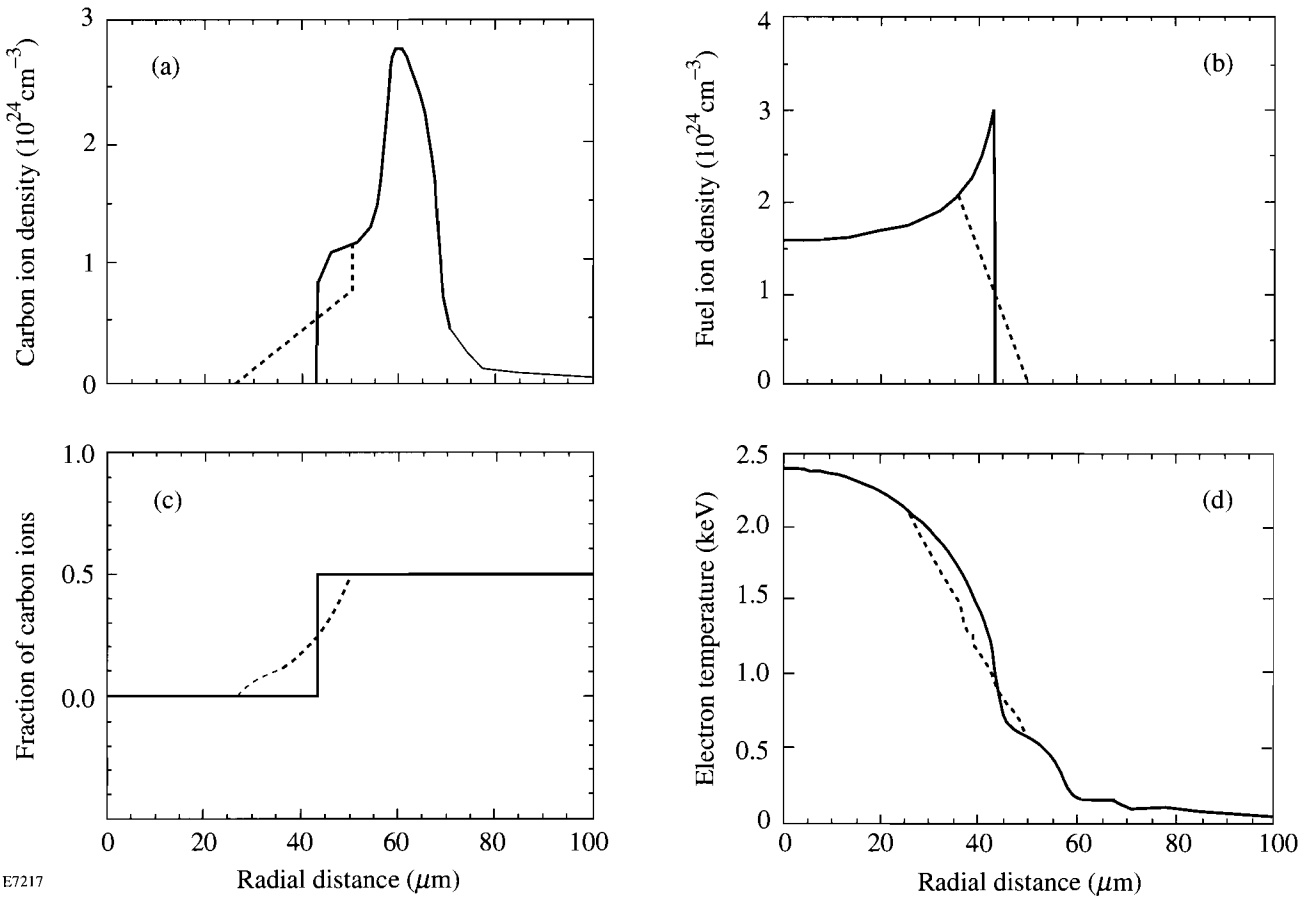

Figure 59.18
Radial profiles in the unmixed (—) and mixed (- - -) target, for $F = 0.4$ mixing: (a) the chosen distribution of carbon ion density (half the CH ion density), (b) the chosen distribution of fuel ions (half of which is D, half T), (c) the calculated distribution of the fraction of carbon ions among all hydrogenic ions (H, D, and T), and (d) the calculated distribution of the electron temperature. The shell-fuel interface position with no mixing is at 42.7 μm.

and 0 at $r = R_s$. A similar behavior is seen by the profile of the average charge.

We next calculate the effect of mixing on the temperature and electron density. We assume that the radial ordering of any two shell elements that moved into the fuel is the same as they had before moving, and likewise for fuel elements. We further assume that both CH or fuel material carry their own temperature as they move to new locations, where their temperature is then averaged with the local temperature (of material that has not moved). For example, the innermost shell cell in the unmixed target is assumed to map onto a region in the mixed target extending from $r = R_s$ outward, until the total mass in that cell is exhausted; a similar transfer holds for all consecutive shell cells within the mixed region. For the fuel, the outermost cell in the unmixed target maps in the mixed target onto the region extending from $r = R_b$ inward, etc. Once the temperatures of the fuel and shell elements in each zone are determined, the final temperature is given by the average of the two, weighted by the corresponding densities. The same applies to both the electron and ion temperatures. The unmixed and mixed electron temperature profiles at peak compression are shown in Fig. 59.18(d). Obviously, colder shell material lowered the temperature of the fuel region it migrated to, whereas hotter fuel material raised the temperature of the shell region it migrated to. Updating the electron density is similar to updating the temperature. The average charge $\langle z \rangle$ in each unmixed shell zone maps onto the corresponding mixed zones as before; the final electron density is given by $N_e = 2\langle z \rangle N_C + N_F$.

The modeling of target mixing, where a given shell layer is doped with a high-Z dopant, follows the same procedure as outlined above. Namely, the dopant material follows the CH element in which it was embedded initially, and the percentage of doping remains the same. The modeling used here does not include self-consistent feedback, i.e., the effect of mixing in one time step upon the hydrodynamics and radiation physics in subsequent steps. The limitations resulting from this simplification will be further discussed below.

Backlighting and Self-Emission Images of Unmixed Targets

Next we study the ability to diagnose mixing through its effect on target images due to both self-emission and backlighting. The problem of backlighting, including that of doped targets, has been studied previously.[4] In Fig. 59.19 we show an image of a doped but unmixed target, at λ = 1.48 Å (the helium-like resonance line of Cu^{+27}), and then show how it changes when mixing is introduced. The total image is due to both self-emission and backlighting (for distances ≳45 μm the self-emission is negligible, and the total image is due to backlighting). The two vertical bars mark the boundaries of the doped region (the left bar also marks the interface). The curves in Fig. 59.19 assume diffraction off a crystal of 4-eV bandwidth (rocking-curve width). As seen, the two image components have comparable intensity, which will be shown below to be essential for the diagnostic method. Without monochromatization, the self-emission will overwhelm the backlighting image and render the method impractical. Thus, if instead of using a monochromator we were to use a filter, the intensity of the monochromatic backlighting radiation (consisting mostly of a single spectral line) will remain about the same. However, the intensity of the continuous self-emission will greatly increase because the filter bandpass will be ~1 keV, as compared to the crystal bandpass of ~4 eV. The spike at r = 43 μm is emitted by the shell's inner surface. It exists because the CH shell has a higher Z than the fuel, but only the inner surface of the shell is hot enough to emit at short wavelengths. With no mixing the spike is too narrow to be easily measurable.

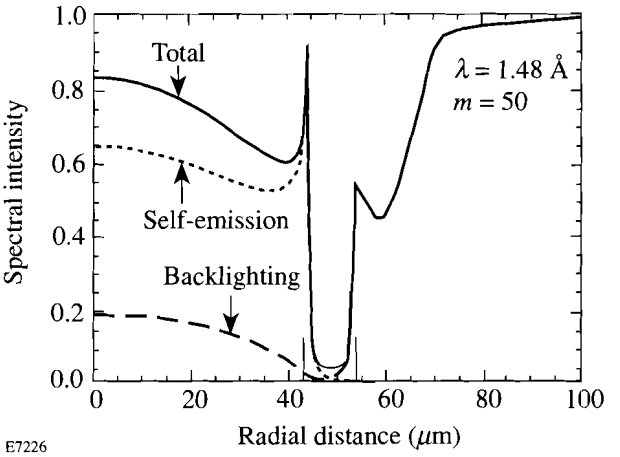

Figure 59.19
The total image due to self-emission and backlighting at E = 8.39 keV (λ = 1.48 Å), with no mixing. The curves are normalized to a spectral intensity of 1.4×10^{20} keV/(keV ns cm^2 Ω), the assumed backlighter x-ray flux at this wavelength. For distances ≳45 μm the self-emission is negligible, and the total image is due to backlighting. The two vertical bars mark the boundaries of the doped region (the left bar is also the interface).

The curves in Fig. 59.19 are normalized to a spectral intensity of 1.4×10^{20} keV/(keV ns cm^2 Ω), the assumed backlighter x-ray flux at this wavelength. This spectral flux level is based on x-ray yield experiments[7] using the helium-like resonance line of Cu^{+27} (λ = 1.48 Å). The image in

Fig. 59.19 is of a doped target, where the inner 2.4 μm have been doped with a high-Z dopant. The motivation for doping is to create a narrower region of absorption so that the delineation of the dense, cold part of the shell be done with greater definition. The initial thickness of the doped layer was chosen so that its width at peak compression (with no mixing) will be resolvable by the imaging instrument. In Fig. 59.19, the width of the absorption ring due to the high-Z dopant (around $r \sim 50$ μm) is about $\Delta r = 8.6$ μm, well within the resolving capability of our x-ray microscopes. Additionally, the outer absorption ring (around $r \sim 58$ μm) is due to absorption in the undoped CH shell. It corresponds to the maximum in the shell density (see Fig. 59.16). On moving to smaller radii, the absorption in the CH decreases partly because of a decrease in the shell density, but mainly because of a rise in the temperature. Figure 59.19 shows clearly the benefit of doping the target: it reduces significantly the width of the absorption region. It also explains the choice of backlighting wavelength: for the absorption in the doped part of the shell to be dominant, the wavelength must be short enough so that the CH absorption is small (see Fig. 59.22 for an image of an undoped target at a longer backlighting wavelength).

Doping was modeled here in a simplified way—by multiplying the total absorption coefficient of the undoped target by a factor m ($m = 50$ in Fig. 59.19). The total calculated absorption coefficient includes bound-free and free-free absorptions.[4] Irrespective of the detailed atomic physics of a high-Z dopant, its final effect is to increase the absorption coefficient and, through it, the local emission (which was related to the absorption coefficient through the Kirchhoff's law). To simulate doping we therefore multiply the absorption coefficient (and thereby also the emission coefficient) by a number m. The only information that is indeterminate here is the quantity of a given type of dopant corresponding to each m.

Calculations with different thicknesses of the doped layer show that the initial thickness of 2.4 μm for the test shot considered here is about optimal. For thinner doped layers the resulting absorption dip may be difficult to resolve, at least in the absence of severe mixing. For thicker doped layers, the outer part of the doped layer is at a low temperature during peak compression. Thus, the temperature where the doped layer absorbs most in Fig. 59.19 is around 400 eV, whereas a thicker doped layer will extend the absorption to regions of temperatures down to ~100 eV, where the absorption is much higher. Such increased absorption causes severe attenuation of the self-emission, particularly from the region near the interface, thus obliterating the sharp rise in intensity seen at $r \sim 45$ μm.

In order to estimate the amount of doping corresponding to a given m we must apply a non-LTE collisional-radiative model to a given high-Z dopant. If the doping is not negligibly small, we must also recompute the hydrodynamic evolution of the doped target. Instead, we make a rough estimate of the doping level corresponding to $m = 50$ if the chosen dopant is chlorine. It has been shown[4] that most of the shell absorption in carbon is due to the bound-free (photo-ionization) process; this is certainly true for any higher-Z dopant. For most of the shell the chlorine ions will be ionized to the helium-like state so that their average Z will be ~15. Since the bound-free absorption coefficient depends on Z like Z^4 (for a given ion density), we estimate that to achieve $m = 50$, the density of chlorine ions should be about the same as that of carbon ions. Higher-Z doping elements will require a lower doping level for the same value of m. Also, a lower value of m can be acceptable if a smaller absorption dip can be tolerated.

Backlighting and Self-Emission Images of Mixed Targets

We now apply the mixing procedure as described earlier to the test target at peak compression and then apply the radiation transport post-processor to calculate the backlighting and self-emission images.

Figures 59.20 and 59.21 show the combined image with and without mixing. The degree of mixing in Fig. 59.20 is $F = 0.2$; in Fig. 59.21 it is $F = 0.4$. The unmixed image is from Fig. 59.19. As mentioned above, comparison with experiments reported previously agreed with a value of $F = 0.2$. Mixing has two effects on the image: (a) the spike of self-emission greatly broadens spatially and moves toward the target center, and (b) its intensity increases dramatically. Both of these effects are caused by CH material moving into higher-temperature regions within the fuel. For $F = 0.2$ the spike moves from $r = 44$ μm to $r = 37$ μm, and its peak intensity increases by about a factor of 12.5. For $F = 0.4$ the spike moves from $r = 44$ μm to $r = 32$ μm, and its peak intensity increases by about a factor of 40. The spike in these two cases broadens to a width of about 5 μm and 9 μm, respectively. The predicted increase in intensity is easily measurable, but the shifts and broadenings are still within the capabilities of the OMEGA Upgrade diagnostics.

The most striking feature in Figs. 59.20 and 59.21 is the fact that the absorption dip is hardly affected by the introduction of mixing. Thus, the measured separation between the emission peak and absorption dip (both of which appear as rings in the two-dimensional image) is a convenient signature of the degree of mixing. As stressed above, the calculations performed here do not account for the feedback effect of the mixing on the

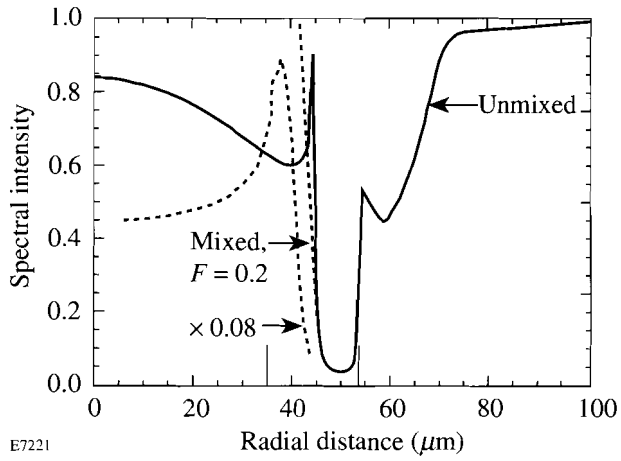

Figure 59.20
The total image at λ = 1.48 Å due to self-emission and backlighting for unmixed and mixed targets (with a degree of mixing $F = 0.2$). The unmixed image is from Fig. 59.19. The curves are normalized to a spectral intensity of 1.4×10^{20} keV/(keV ns cm^2 Ω). The two vertical bars mark the boundaries of the doped region (in the mixed target). The shell-fuel interface position with no mixing is at 42.7 μm.

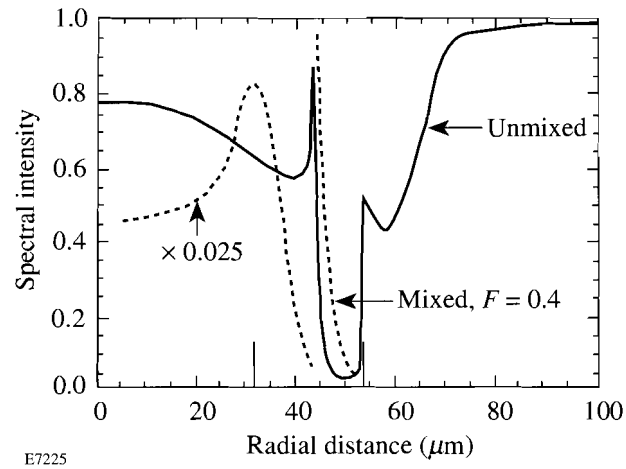

Figure 59.21
The total image at λ = 1.48 Å due to self-emission and backlighting for unmixed and mixed targets (with a degree of mixing $F = 0.4$). The unmixed image is from Fig. 59.19. The curves are normalized to a spectral intensity of 1.4×10^{20} keV/(keV ns cm^2 Ω). The two vertical bars mark the boundaries of the doped region (in the mixed target). The shell-fuel interface position with no mixing is at 42.7 μm.

hydrodynamic and thermodynamic target evolution. The main effect of such a feedback is expected to be the lowering of the temperature in the fuel region due to radiation cooling by the high-Z contaminant (which includes CH material and any dopant assumed in the initial target). This cooling will reduce the intensity of the emission peak. However, the general statement will still be valid, that the absorption dip is a signature of the position of the compressed shell, whereas the emission peak is a measure of the penetration of shell material into the fuel. *Thus, a very useful comparison of experiment and theoretical predictions can be obtained if the imaging includes a backlighting component in addition to the self-emission image.*

Finally, we discuss the effect of mixing on the backlighting image of undoped targets. Since, as we have seen earlier, the absorption of 1.48-Å radiation in the test target with no doping is very small, we increase the backlighting wavelength to 2.62 Å (the wavelength of the helium-like resonance line of Ti^{+20}). Figure 59.22 shows the combined backlighting and self-emission images for two degrees of mixing, $F = 0.2$ and $F = 0.4$. The spectral flux is normalized to that expected[7,8] from a titanium backlighter: 7.0×10^{20} keV/(keV ns cm^2 Ω). Undoped targets give rise to a broader, less-well-defined absorption peak. However, the target fabrication is simpler, and, due to the longer wavelength, the intensity is higher. Comparing Fig. 59.22 to Figs. 59.20 and 59.21 shows that the position of the emission peaks for a given F value is almost the same for the two different wavelengths. However, the increase in intensity is not as dramatic as with the shorter wavelength. As recalled, the increase in intensity of the self-emission is due to shell material moving into higher temperature regions in the core. The intensity is governed by factors of the type $\exp[-(E/kT)]$, where E is the photon energy. Thus, when E is higher (as is the case in Figs. 59.20 and 59.21), the intensity increases faster with increasing temperature.

The fact that the peak position is about the same for the two wavelengths (for the same level of mixing) supports the contention that a fully consistent calculation of the mixed target evolution should result in a similar shift of the emission peak. Radiation cooling will certainly reduce the emission peak intensity, but the peak position will depend primarily on the length of mixing and less on the temperature. The peak appears roughly at the position of maximum penetration of the shell material into the fuel because the temperature there is maximal over the penetration depth. We have calculated images such as in Figs. 59.20–59.22 for increasing F values, up to the maximum of F ~0.7; at that value of F the free-fall line (see Fig. 59.17) reaches the target center by the time of peak compression. In all these cases the absorption dip position and depth remain about the same. This means that the observation of significant deviations from the predicted characteristics of the absorption ring is evidence of more severe instability, such

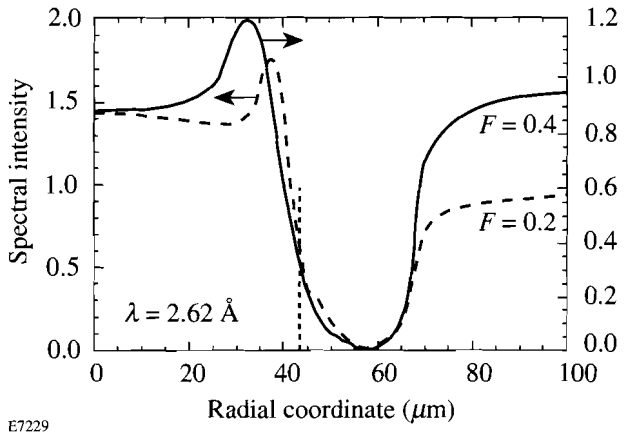

Figure 59.22
The combined backlighting and self-emission image of the test target with no doping, at $\lambda = 2.62$ Å, and two degrees of mixing: $F = 0.2$ and $F = 0.4$. The curves are normalized to a spectral intensity of 7.0×10^{20} keV/(keV ns cm^2 Ω). The vertical dashed bar marks the position the shell-fuel interface would have without mixing.

as shell disruption on the way in, due to initial nonuniformity. Finally, the measured absorption depth (i.e., the attenuation of backlighting radiation) can be used for comparison with predictions. This attenuation depends both on the shell temperature and the shell $\rho\Delta r$. The position of the absorption ring can be used to deduce the fuel compression and the presence of low-order nonuniformity of the compressed core.

ACKNOWLEDGMENT

This work was supported by the U.S. Department of Energy Office of Inertial Confinement Fusion under Cooperative Agreement No. DE-FC03-92SF19460, the University of Rochester, and the New York State Energy Research and Development Authority. The support of DOE does not constitute an endorsement by DOE of the views expressed in this article.

REFERENCES

1. J. D. Lindl, R. L. McCrory, and E. M. Campbell, Phys. Today **45**, 32 (1992).
2. O. L. Landen, W. K. Levedahl, and T. R. Dittrich, Bull. Am. Phys. Soc. **38**, 2083 (1993).
3. B. Yaakobi, F. J. Marshall, Q. Su, and R. Epstein, to appear in the Journal of X-Ray Science and Technology.
4. Laboratory for Laser Energetics LLE Review **58**, NTIS document No. DOE/SF/19460-17, 1994 (unpublished), p. 57.
5. C. P Verdon, R. L. McCrory, R. L. Morse, G. R. Baker, D. I. Meiron, and S. A. Orszak, Phys. Fluids **25**, 1653 (1982).
6. D. L. Youngs, Physica **12D**, 32 (1984); S. W. Haan, Phys. Rev. A **39**, 5812 (1989); N. Freed, D. Ofer, D. Shvarts, and S. A. Orszag, Phys. Fluids A **3**, 912 (1991).
7. B. Yaakobi, P. Bourke, Y. Conturie, J. Delettrez, J. M. Forsyth, R. D. Frankel, L. M. Goldman, R. L. McCrory, W. Seka, J. M. Soures, A. J. Burek, and R. E. Deslattes, Opt. Commun. **38**, 196 (1981).
8. D. L. Matthews *et al.*, J. Appl. Phys. **54**, 4260 (1983).

Evaluation of Cosmic Rays for Use in the Monitoring of the MEDUSA Scintillator–Photomultiplier Diagnostic Array

Current and planned ICF implosion experiments require the detailed measurement of physical conditions on the imploded core. Glass and plastic shells filled with D_2 open a window into the core by measuring the ratio of the various fusion reactions occurring during the implosion.[1] The number of each reaction is measured by characterization of the energy spectrum for the penetrating reaction products (either neutrons or protons). The measurement of the neutron energy spectrum around the 3-MeV neutron from the $d(d,He^3)n$ reaction and around the 14-MeV neutron from the $d(t,He^4)n$ reaction has evolved into the most used nuclear core diagnostic.

For a target filled with D_2, the $d(t,He^4)n$ fusion reaction is a secondary process and will generate about 10^{-3} times less neutrons than the primary D_2 reaction, $d(d,He^3)n$. Large area detectors that measure the neutron energy spectrum by the time-of-flight (TOF) method have become the standard for determination of the details of the 14-MeV neutron spectrum.[2] Adaptations of this instrument are being built to also measure the neutron spectrum from the various primary fusion reactions with high energy resolution.[3] The Laboratory for Laser Energetics at the University of Rochester is building such a detector for implosion experiments planned for the OMEGA Upgrade. This diagnostic, a multi-element detector using a scintillator array (MEDUSA),[4] will be used to study the details of the neutron energy spectrum around the 14-MeV neutron emitted from the $d(t,He^4)n$ secondary reaction.

MEDUSA

The MEDUSA diagnostic consists of 960 separate scintillator-photomultiplier detectors arranged in an array with 32 columns and 30 rows. This array is located in a separate instrumentation room 19 m from the center of the target chamber. At this distance the time-of-flight for the 14-MeV neutrons will be 370 ns after their creation. The center of the target chamber is about 9.3 m above the center of the instrument. This requires that the array be tilted at an angle of 26° relative to the vertical so that the detector plane is normal to the line connecting the center of the array with the center of the target chamber. The active area of the array is 3.87 m^2, resulting in a subtended solid angle of 0.011 sterad. Each element of this array is constructed from a solid block of NE 110 scintillator 6.35 cm high × 6.25 cm wide × 7.62 cm deep. A Thorn EMI 9257B photomultiplier is attached to the rear of the scintillator block. A schematic for each of the individual detection channels is shown in Fig. 59.23.

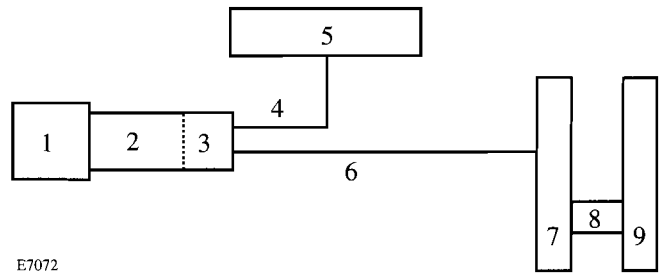

Figure 59.23
Schematic of each MEDUSA scintillator-photomultiplier channel.

Each MEDUSA channel (Fig. 59.23) consists of nine separate components, giving a total of 8640 components for the whole diagnostic array. All such large arrays require that all of these individual pieces continue to work during the lifetime of the instrument. The large neutron scintillator array (LaNSA) at the Lawrence Livermore National Laboratory[2] uses radioactive sources placed in each channel to monitor individual channel performance. LaNSA is a horizontal array at the bottom of a deep well, which makes the use of naturally occurring ionizing radiation difficult. The LLE MEDUSA array is nearly vertical and, as such, is a prime candidate for the use of cosmic rays as a source of ionizing radiation to monitor channel performance. The calculation of the counting rates and signal levels will determine if this technique will work.

Cosmic Rays

The flux of cosmic rays incident onto the surface of the earth is known to be 110 particles/(m^2 str s),[5] about 73% [80 particles/(m^2 str s)] of which are penetrating particles. Most of the particles at the earth's surface are muons. Muons are

generated from the decay of pions created when a high-energy particle in space interacts with a nucleus in the earth's atmosphere. The muons have sufficient energy to be classified as minimum ionizing particles, which are particles that have energies greater than or equal to the energy of a particle at the minimum of the *dE/dx* ionization loss curve. Counting rates for the detectors in the MEDUSA array are calculated to be 2.9 particles/h for a single column of 30 scintillator-photomultiplier channels. This gives a total counting rate of 93.2 particles/h for all 32 columns in the diagnostic array. An overnight run of 16 h will result in 50 counts for each detector—enough counts to determine the status of all components in the diagnostic.

A minimum ionizing particle passing through a NE 110 scintillator has an energy loss (*dE/dx*) of 2.0 MeV/cm. The minimum path length of a cosmic ray detected by the MEDUSA scintillator-photomultiplier channel is 6.35 cm, resulting in a total energy deposition from the cosmic ray of 12.7 MeV. This is very well matched to the maximum energy deposited by a neutron of 13.7 MeV. Since there is sufficient signal to detect a neutron, there will be enough signal to detect a cosmic ray.

A test on a small subarray will determine if both a sufficient count rate and signal level exist to detect cosmic rays in the MEDUSA diagnostic array.

Cosmic Ray Tests

A smaller subarray of detectors was constructed to simulate the larger MEDUSA diagnostic. A schematic of this setup is shown in Fig. 59.24. It is constructed from a 4 × 4 array of MEDUSA scintillator-photomultiplier channels and two separate trigger counters. The trigger counters are used to establish the presence of a cosmic ray that has passed through the detectors in the subarray. Sixteen detectors were used from the MEDUSA diagnostic for the test so that the test was conducted with a sample of detectors used in the primary array. The trigger counters are scintillator-photomultiplier detectors constructed for a high-energy physics experiment conducted at the Fermi National Accelerator Laboratory in the 1970's and 1980's. The scintillator in the trigger counters is NE 111, 8.89 cm long × 7.62 cm deep × 1.27 cm thick. An Amperex 56 AVP is used as the photomultiplier. The voltages required by the trigger counters were 1750 V and 2200 V. The size of the trigger counters allowed tests to be conducted on four of the 16 subarray detectors during a single data-acquisition session.

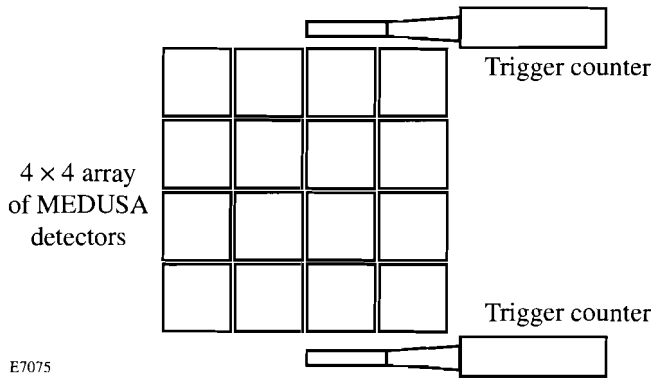

Figure 59.24
Schematic of the subarray used to test the cosmic-ray count rate concept for monitoring the MEDUSA diagnostic.

The trigger counters and the subarray detectors were connected to the electronics shown schematically in Fig. 59.25. The trigger counters were connected to a discriminator located in a NIM bin with the threshold set to 100 mV. The discriminator outputs were used as inputs for a coincidence logic unit. This logic unit gave an output when both discriminators detected a pulse above threshold to establish the presence of a particle passing through both trigger counters. The output of the logic unit was used as the start trigger for a time-to-digital converter (TDC) and as a gate signal for the charge-to-digital converter (QDC). The MEDUSA scintillator-photomultiplier outputs are fed into a CAMAC discriminator and a CAMAC QDC. The discriminators have computer-selectable thresholds. Outputs from the CAMAC discriminator were used as the stop triggers for the TDC. CAMAC scalars counted outputs from the trigger counter discriminators, logic unit, TDC start trigger, and MEDUSA channel discriminator. The CAMAC crate was controlled with an IEEE 488 interfaced controller connected to a Macintosh computer using National Instruments' Lab View as the data-acquisition software. This electronics and software configuration allowed a great deal of flexibility in the tests conducted with this subarray.

Three primary tests were conducted with the 4 × 4 subarray of MEDUSA detectors: (1) determination of the count rate as a function of the discriminator threshold; (2) measurement of the charge distribution as a result of cosmic rays depositing energy in the scintillators; and (3) studying the temporal histogram from the CAMAC TDC stop trigger generated when a cosmic ray is detected by the MEDUSA scintillator-

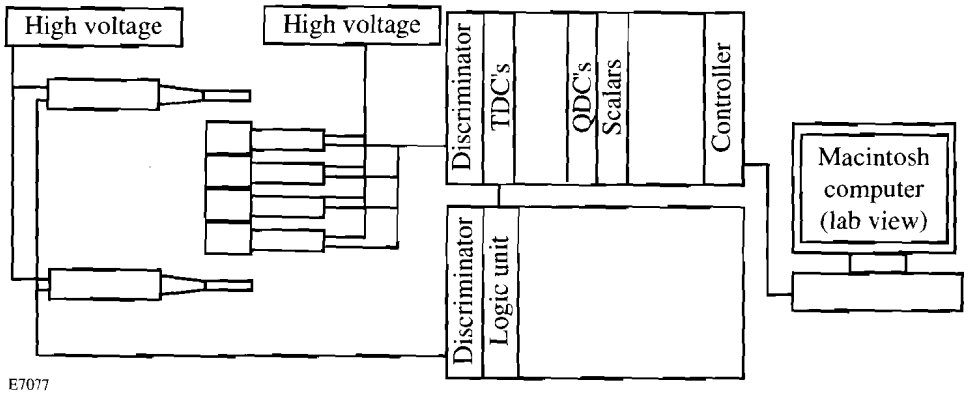

Figure 59.25
Schematic of the electronics used to test the cosmic-ray monitoring concept on the MEDUSA subarray.

photomultiplier channel. The output signal uniformity of the four channels tested is an indication of the expected performance for the whole array during a cosmic-ray test sequence. The results from the above measurements are shown in Figs. 59.26–59.28.

Data from the counter threshold measurement is shown in Fig. 59.26. The number of counts in 1000 s is plotted as a function of the CAMAC discriminator threshold. Four of the MEDUSA subarray detectors are plotted on the same graph. The minimum discriminator threshold is 20 mV, and the maximum threshold is 1020 mV. The first important observation is that all four detectors show nearly identical performance. There are two regions evident in the threshold data. The region below 50 mV is dominated by the noise from the scintillator-photomultiplier detector. These data are fit by an exponential, and the function can be integrated to determine the probability for a noise count during the active time of a neutron spectral measurement. All four channels show a 5% probability that there will be a noise trigger in all 960 detectors for a 1-μs diagnostic time window for a discriminator threshold of 17 mV. These data are being used to determine the thresholds for all 960 MEDUSA channels.

The results from the charge distribution test are shown in Fig. 59.27. As in the previous data, it is evident that all four counters have a nearly identical charge spectrum from cosmic ray energy deposition. There is a well-defined peak that is well separated from any noise. All four detectors show a peak at around 400 counts, corresponding to an integrated charge of 100 pC. The signal was attenuated by 2 before it was connected to the QDC. The total integrated charge from the detector is 200 pC. It was shown previously that a cosmic-ray event simulates a 13.7-MeV neutron that deposits 12.7 MeV in the scintillator. The data from the charge spectrum imply that a 13.7-MeV neutron will yield a total output charge of 216 pC.

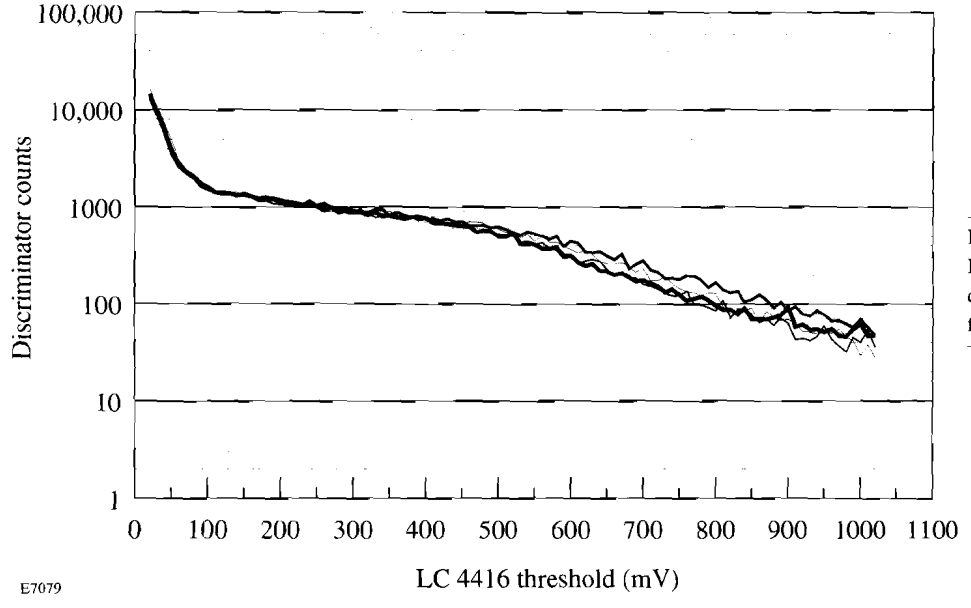

Figure 59.26
Plot of the number of counts from the discriminator verses the discriminator threshold for the MEDUSA channel subarray.

The uniformity of the spectrum from each of the four detectors will allow the cosmic-ray data to correlate to the calibration data from the nuclear fusion product source used to check selected detectors.[6] The cosmic-ray data will thus be able to serve not only as a monitor of the performance of each channel but also as a check of the energy calibration for the detectors.

The TDC data, plotted in Fig. 59.28, are nearly identical for each of the channels, as was the case in the two previous tests. All four channels show a peak around 20 ns. This time is determined by the added delay in each channel to insure that the stop triggers arrive after the start triggers. The width [full-width at half-maximum (FWHM)] for all of the channels is less than 0.5 ns, which is equivalent to one count of the TDC output. The consistency of these data indicates that it will be possible to use the cosmic ray data to check the performance of the TDC's used on the MEDUSA diagnostic.

Summary

The results from the initial tests to determine the utility of using cosmic rays to monitor the performance of the MEDUSA detectors indicate that this source of ionizing radiation is quite suitable. All tests imply that the data from the cosmic-ray monitoring sessions can be used to not only monitor the channels but also check their calibrations. The calculated counting rate for the subarray was 392 particles/h; the measured rate was 349 particles/h. MEDUSA's calculated counting rate of 93.2 particles/h should be close to the actual

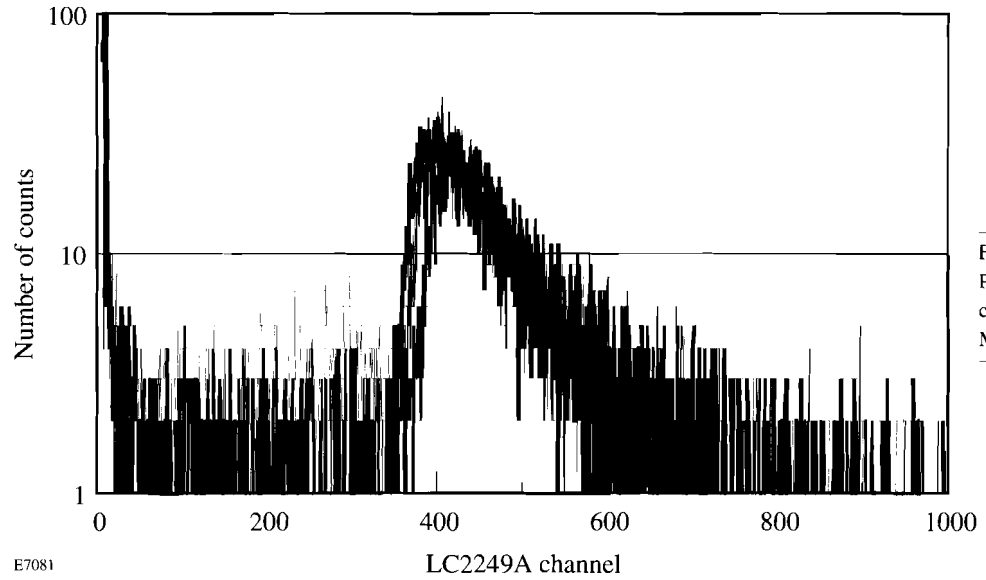

Figure 59.27
Pulse-height spectrum from the CAMAC charge-to-digital converter connected to the MEDUSA channel subarray.

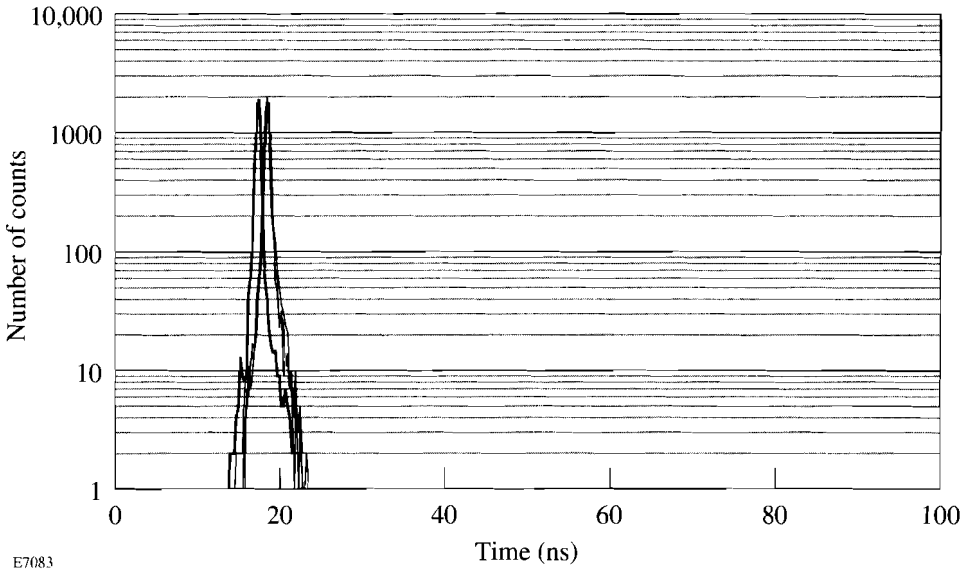

Figure 59.28
Temporal count spectrum from the CAMAC time-to-digital converter connected to the MEDUSA channel subarray.

counting rate when the full detector is completed and ready for testing. There is excellent agreement with the expected signal levels and temporal stop trigger jitter. Radiation sources or optically coupled sources should not be required to monitor the individual channels. To test the MEDUSA diagnostic, only a data-acquisition routine will be required to collect and analyze cosmic-ray events when the detector is not needed to acquire data from an ICF implosion.

ACKNOWLEDGMENT

This work was supported by the U.S. Department of Energy Office of Inertial Confinement Fusion under Cooperative Agreement No. DE-FC03-92SF19460 and the University of Rochester. The support of DOE does not constitute an endorsement by DOE of the views expressed in this article.

REFERENCES

1. T. E. Blue and D. B. Harris, Nucl. Sci. Eng. **77**, 463 (1981).
2. M. D. Cable, S. P. Hatchett, and M. B. Nelson, Rev. Sci. Instrum. **63**, 4823 (1992).
3. R. E. Chrien, presented at the *APS 10th High-Temperature Plasma Diagnostics Conference*, Rochester, NY, 8–12 May 1994.
4. R. L. Kremens and M. A. Russotto, presented at the *APS 33rd Annual Meeting of the Division of Plasma Physics*, Tampa, FL, 4–8 November 1991.
5. M. Aguilar-Benitez *et al.*, in the *Particle Properties Data Booklet*, from the *Review of Particle Properties*, Physical Review **D45**, Part 2 (June 1992).
6. S. Padalino, B. Emerling, P. King, M. Rodgers, and R. Kremens, presented at the *APS 10th High-Temperature Plasma Diagnostics Conference*, Rochester, NY, 8–12 May 1994.

PUBLICATIONS AND CONFERENCE PRESENTATIONS

Publications

S. Alexandrou, C.-C. Wang, M. Currie, R. Sobolewski, and T. Y. Hsiang, "Loss and Dispersion at Subterahertz Frequencies in Coplanar Waveguides with Varying Ground-Plane Widths," in *Technologies for Optical Fiber Communications*, edited by G. J. Brown *et al.* (SPIE, Bellingham, WA, 1994), Vol. 2149, pp. 108–118.

S. Alexandrou, C.-C. Wang, R. Sobolewski, and T. Y. Hsiang, "Generation of Subpicosecond Electrical Pulses by Nonuniform Illumination of GaAs Transmission Line Gaps," IEEE J. Quantum Electron. **30**, 1332 (1994).

X. D. Cao, G. P. Agrawal, and C. J. McKinstrie, "Self-Focusing of Chirped Optical Pulses in Nonlinear Dispersive Media," Phys. Rev. A **49**, 4085 (1994).

X. D. Cao and D. D. Meyerhofer, "Nonlinear Birefringence of Optical Fibers," Opt. Commun. **109**, 151 (1994).

E. M. Epperlein, "Fokker-Planck Modeling of Electron Transport in Laser-Produced Plasmas," Laser Part. Beams **12**, 257 (1994).

E. M. Epperlein, "Implicit and Conservative Difference Scheme for the Fokker-Planck Equation," J. Comput. Phys. **112**, 291 (1994).

E. M. Epperlein and R. W. Short, "Comments on 'Theory and Three-Dimensional Simulation of Light Filamentation in Laser-Produced Plasmas' [Phys. Fluids B 5, 2243 (1993)]," Phys. Plasmas **1**, 1364 (1994).

P. Gierlowski, G. Jung, W. Kula, S. J. Lewandowski, B. Savo, R. Sobolewski, A. Tebano, and A. Vecchione, "Low Frequency Voltage Noise in Current Biased HTSC Thin Films," Physica B **194–196**, 2043 (1994).

T. Gong, J. F. Young, G. W. Wicks, P. J. Kelly, and P. M. Fauchet, "Hot-Carrier Dynamics Near the Fermi Edge of N-Doped GaAs," Semicond. Sci. Technol. **9**, 459 (1994).

T. Gong and P. M. Fauchet, "Carrier-Carrier Interactions in GaAs Investigated by Femtosecond Spectroscopy," in *Ultrafast Pulse Generation and Spectroscopy* (SPIE, Bellingham, WA, 1993), Vol. 1861, pp. 227–236. (invited)

D. Gupta, "A New Optically Triggered Superconducting Opening Switch for High-Power Applications," in *Research Reports of the Link Energy Fellows*, edited by B. J. Thompson (The University of Rochester Press, Rochester, NY, 1994), Vol. 9, pp. 25–41.

D. Gupta, W. R. Donaldson, and A. M. Kadin, "Fast Inductively Coupled Superconducting Opening Switch Triggered by Short Laser Pulses," in the *Proceedings of the Ninth IEEE International Pulsed Power Conference* (IEEE, New York, 1993), pp. 131–133.

E. M. Korenic, S. D. Jacobs, J. K. Houghton, F. Kreuzer, and A. Schmid, "Nematic Polymer Liquid-Crystal Waveplate for High-Power Lasers at 1054 nm," Appl. Opt. **33**, 1889 (1994).

Y. Kostoulas, P. M. Fauchet, T. Gong, B. C. Tousley, G. W. Wicks, and P. Cooke, "Femtosecond Carrier Dynamics in Low-Temperature-Grown III–V Seminconductors," in *Ultrafast Phenomena in Semiconductors*, edited by D. K. Ferry and H. M. Van Driel (SPIE, Bellingham, WA, 1994), Vol. 2142, pp. 100–109.

Y. Kostoulas, T. Gong, and P. M. Fauchet, "Investigation of Carrier-Carrier Scattering by Three-Pulse Pump-Probe Spectroscopy," Semicond. Sci. Technol. **9**, 462 (1994).

W. Kula and R. Sobolewski, "Electric-Field Effect in Partially Deoxygenated YBCO Thin Films," Physica B **194–196**, 2083 (1994).

W. Kula and R. Sobolewski, "Electric-Field-Effect Devices Based on Partially Oxygen-Depleted, Superconducting Y-Ba-Cu-O Thin Films," in *Advances in Cryogenic Engineering*, edited by R. P. Reed *et al.* (Plenum Press, New York, 1994), Vol. 40, pp. 377–383.

W. Lang, W. Kula, and R. Sobolewski, "Superconducting Fluctuations: Paraconductivity, Excess Hall Effect, and Magnetoconductivity in 2223-BiSrCaCuO Thin Films," Physica B **194–196**, 1643 (1994).

A. I. Lobad, P. J. Rodney, B. C. Tousley, S. M. Mehta, and P. M. Fauchet, "The Starting Mechanism in Coupled-Cavity, Mode-Locked Laser Systems," in *Generation, Amplification, and Measurement of Ultrashort Laser Pulses*, edited by R. P. Trebino and I. A. Walmsley (SPIE, Bellingham, WA, 1994), Vol. 2116, pp. 109–117.

A. I. Lobad, P. J. Rodney, S. M. Mehta, B. C. Tousley, and P. M. Fauchet, "The Starting Mechanism in Coupled-Cavity Modelocked Laser Systems," IEEE J. Quantum Electron. **30**, 812 (1994).

F. J. Marshall, J. A. Delettrez, R. Epstein, and B. Yaakobi, "Diagnosis of Laser-Target Implosions by Space-Resolved Continuum Absorption X-Ray Spectroscopy," Phys. Rev. E **49**, 4381 (1994).

W. N. Maung, D. P. Butler, W. Xiong, W. Kula, and R. Sobolewski, "Propagation Characteristics of Monolithic Y-Ba-Cu-O Coplanar Strip Transmission Lines Fabricated by Laser Writing Patterning Technique," IEEE Microw. Guid. Wave Lett. **MGWL-4**, 132 (1994).

L. Mu and W. R. Donaldson, "Simulating Photoconductive Switches in a Microwave Transmission Line," in the *Proceedings of the Ninth IEEE International Pulsed Power Conference* (IEEE, New York, 1993), pp. 629–632.

J. K. Samarabandu, R. Acharya, C. D. Edirisinghe, P. C. Cheng, H. Kim, T. H. Lin, R. G. Summers, and C. E. Musial, "Analysis of Multi-Dimensional Confocal Images, in *Biomedical Image Processing II*, edited by A. C. Bovik and V. Howard (SPIE, Bellingham, WA, 1991), Vol. 1450, pp. 296–322.

R. Sobolewski, L. Shi, T. Gong, W. Xiong, X. Weng, Y. Kostoulas, and P. M. Fauchet, "Femtosecond Optical Response of Y-Ba-Cu-O Thin Films and Their Applications in Optoelectronics," in *High-Temperature Superconducting Detectors: Bolometric and Nonbolometric*, edited by M. Nahum and J.-C. Villegier (SPIE, Bellingham, WA, 1994), Vol. 2159, pp. 110–120.

R. Sobolewski, W. Xiong, W. Kula, and B. McIntyre, "Electrical and Structural Properties of the YBCO Superconducting-Semiconducting Interface," Physica B **194–196**, 2143 (1994).

C. J. Twomey, S.-H. Chen, T. N. Blanton, A. Schmid, and K. L. Marshall, "Poly[(Methylene Oxide)Oligo(Ethylene Oxide)] Vs. Poly(Ethylene Oxide) as Hosts for Neodymium Compounds," J. Polym. Sci. B, Polym. Phys. **32**, 1687 (1994).

C. J. Twomey, S.-H. Chen, T. N. Blanton, A. W. Schmid, and K. L. Marshall, "Stoichiometry and Morphology in Terbium Nitrate-Poly(Ethylene Oxide) Macromolecular Complex," J. Polym. Sci. B, Polym. Phys. **32**, 1573 (1994).

C.-C. Wang, S. Alexandrou, D. Jacobs-Perkins, and T.Y. Hsiang, "Comparison of the Picosecond Characteristics of Silicon and Silicon-on-Sapphire Metal-Semiconductor-Metal Photodiodes," Appl. Phys. Lett. **64**, 3578 (1994).

C.-C. Wang, S. Alexandrou, D. Jacobs-Perkins, and T. Y. Hsiang, "Picosecond Characteristics of Silicon-on-Insulator Metal-Semiconductor-Metal Photodiodes," in *Technologies for Optical Fiber Communications*, edited by G. J. Brown *et al.* (SPIE, Bellingham, WA, 1994), Vol. 2149, pp. 271–275.

W. Xiong, W. Kula, and R. Sobolewski, "Fabrication of High-T_c Superconducting Electronic Devices Using the Laser-Writing Patterning Technique," in *Advances in Cryogenic Engineering* (Plenum Press, New York, 1994), Vol. 40A, pp. 385–391.

W. Xiong, W. Kula, R. Sobolewski, W. N. Maung, and D. P. Butler, "Monolithic Y-Ba-Cu-O Structures Fabricated Using the Laser-Writing Patterning Technique," Supercond. Sci. Technol. **7**, 300 (1994).

J. F. Young, T. Gong, P. J. Kelly, and P. M. Fauchet, "Carrier-Carrier Scatterings within Athermol Distributions," Semicond. Sci. Technol. **9**, 465 (1994).

Forthcoming Publications

J. J. Armstrong and T. J. Kessler, "Holographic Generation of High-Efficiency, Large-Aperture, Transmission Diffraction Gratings," to be published in *Applied Optics A*.

R. Betti, V. Goncharov, R. L. McCrory, E. Turano, and C. P. Verdon, "Multiple Cutoff Wave Numbers of the Ablative Rayleigh-Taylor Instability," to be published in *Physical Review Letters*.

T. R. Boehly, R. S. Craxton, T. H. Hinterman, P. A. Jaanimagi, J. H. Kelly, T. J. Kessler, R. L. Kremens, S. A. Kumpan, S. A. Letzring, R. L. McCrory, S. F. B. Morse, W. Seka, S. Skupsky, J. M. Soures, and C. P. Verdon, "The Upgrade to the OMEGA Laser System," to be published in the *Proceedings of the American Nuclear Society*.

D. K. Bradley, P. M. Bell, O. L. Landen, J. D. Kilkenny, and J. Oertel, "Development and Characterization of a Pair of 30–40 ps X-Ray Framing Cameras," to be published in the *Review of Scientific Instruments*.

X. D. Cao, D. D. Meyerhofer, and G. P. Agrawal, "Optimization of Optical Beam Steering in Nonlinear Kerr Media Via Spatial Phase Modulation," to be published in the *Journal of the Optical Society of America B*.

X. D. Cao and D. D. Meyerhofer, "All-Optical Switching Via Collisions of Spatial Vector Solitons," to be published in *Optics Letters*.

X. D. Cao and D. D. Meyerhofer, "Frequency-Domain Interferometer for Measurement of the Polarization Modal Dispersion in Single-Mode Optical Fibers," to be published in *Optics Letters*.

S. H. Chen and S. Krishnamurthy, "Some Fundamental Issues Governing Thermotropic Chiral Nematic Copolymers," to be published in the *Proceedings of the 42nd Society for Polymer Science*, Kyoto, Japan, 31 May–2 June 1993.

C. T. Cotton, "The Design of an All-Spherical, Three-Mirror, Off-Axis Telescope Objective," to be published in the *OSA Proceedings of the International Optical Design Conference '94*.

M. J. Cumbo and S. D. Jacobs, "Determination of Near-Surface Forces in Optical Polishing Using Atomic Force Microscopy," to be published in *Nanotechnology*.

J. A. Delettrez, D. K. Bradley, and C. P. Verdon, "The Role of the Rayleigh-Taylor Instability in Laser-Driven Burnthrough Experiments," to be published in *Physics of Fluids B*.

W. R. Donaldson and L. Mu, "Effect of Illumination Uniformity on GaAs Photoconductive Switches," to be published in the *IEEE Journal of Quantum Electronics*.

E. M. Epperlein and R. W. Short, "Generalized Electron Fluid Equations in the Presence of Laser Irradiation," to be published in *Physics of Plasmas*.

E. M. Epperlein and R. W. Short, "Nonlocal Electron Transport in the Presence of High-Intensity Laser Irradiation," to be published in *Physical Review E*.

D. Fried, R. E. Glena, J. D. B. Featherstone, and W. Seka, "The Nature of Light Scattering in Dental Enamel and Dentin at Visible and Near Infrared Wavelengths," to be published in *Applied Optics*.

W. Gob, W. Lang, W. Kula, and R. Sobolewski, "Transport Properties and Superconducting Fluctuations in Oxygen Deficient Y-Ba-Cu-O Thin Films," to be published in *Physica C*.

D. Gupta, W. R. Donaldson, and A. M. Kadin, "A Laser-Triggered, Inductive Opening Switch Using High-Temperature Superconducting Thin Films," to be published in *Advances in Cryogenic Engineering*.

D. Gupta, W. R. Donaldson, and A. M. Kadin, "Energy Extraction from Superconducting Magnets Using Optically Activated $YBa_2Cu_3O_{7-x}$ Switches," to be published in *Optically Activated Switching IV*.

J. W. Herman, H. E. Elsayed-Ali, and E. A. Murphy, "Time-Resolved Structural Studies of the Low-Index Faces of Lead," to be published in *Physical Review B*.

P. A. Jaanimagi, R. C. Elton, B. L. Welch, Y. Leng, and H. R. Griem, "Extending X-Ray Streak Camera Operation to VUV Wavelengths," to be published in the *Review of Scientific Instruments*.

S. D. Jacobs, K. L. Marshall, and A. Schmid, "Liquid Crystals for Laser Applications," to be published in the *CRC Handbook of Laser Science and Technology, Supplement 2: Optical Materials.*

H. Kim, J. M. Soures, and P.-C. Cheng, "Confocal Microscopic Characterization of Laser-Fusion Target," to be published in the *Proceedings of the 39th AVS National Symposium and Topical Conferences*, Chicago, IL, 9–13 November 1992.

E. M. Korenic, K. L. Marshall, and J. A. Maiolo, "Blending Polysiloxane 'Glass Resins' to Produce Optical Films with a Specific Refractive Index," to be published in *Optics and Photonics News.*

W. Kula and R. Sobolewski, "Effect of Hydrogen Doping on Electrical Properties of Y-Ba-Cu-O Thin Films," to be published in *Physica C.*

B. S. W. Kuo and A. W. Schmid, "Effects of Thin-Film Thermal Conductivity on the Optical Damage Threshold of a-Si Film on c-Si Substrate at 1064 nm," to be published in the *Journal of Applied Physics.*

Y. Lin and T. J. Kessler, "Raman Scattering: A Four-Dimensional System," to be published in *Applied Optics.*

R. S. Marjoribanks, F. W. Budnik, H. Chen, and D. D. Meyerhofer, "Plasma Electron Temperature in Picosecond Laser Plasmas from Quasi-Steady Ratio of Isoelectronic Lines," to be published in *Physical Review Letters.*

R. L. McCrory, "Progress Toward Ignition with Direct Drive," to be published in *Concerning Major Systems in Science and Technology.*

P. W. McKenty, S. Skupsky, J. H. Kelly, and C. T. Cotton, "Numerical Investigation of the Self-Focusing of Broad-Bandwidth Laser Light with Applied Angular Dispersion," to be published in the *Journal of Applied Physics.*

C. J. McKinstrie, R. Betti, R. E. Giacone, T. Kolber, and J. S. Li, "Two-Dimensional Stimulated Brillouin Scattering," to be published in *Physical Review E.*

C. I. Moore, J. P. Knauer, and D. D. Meyerhofer, "Relativistic Ponderomotive Acceleration of Electrons from a Laser Focus," to be published in the *Bulletin of the American Physical Society.*

A. Okishev, M. D. Skeldon, and W. Seka, "Optical Pulse Compression by Stimulated Scattering for Pulse-Shaping Applications in the OMEGA Upgrade Laser," to be published in the *Proceedings of the Conference on Lasers and Electro-Optics (1994).*

S. Papernov and A. W. Schmid, "Atomic Force Microscopy Studies of Laser-Triggered Morphology Changes in Y_2O_3 Monolayer Coatings," to be published in *SPIE's Proceedings of the Annual Symposium on Optical Materials for High Power Lasers.*

S. Papernov and A. W. Schmid, "Atomic Force Microscopy Observations of Water-Induced Morphological Changes in Y_2O_3 Monolayer Coatings," to be published in *SPIE's Proceedings of the Annual Symposium on Optical Materials for High Power Lasers.*

J. Peatross, J. L. Chaloupka, and D. D. Meyerhofer, "High-Order Harmonic Generation with an Annular Laser Beam," to be published in *High Field Interactions and Short Wavelength Generation (1994).*

J. Peatross, J. L. Chaloupka, and D. D. Meyerhofer, "High-Order Harmonic Generation with an Annular Laser Beam," to be published in *Optics Letters.*

J. Peatross and D. D. Meyerhofer, "The Angular Distribution of High-Order Harmonics Emitted from Rare Gases at Low Density," to be published in *Physical Review Letters.*

J. Z. Roach, A. Ninkov, S. W. Swales, and T. Morris, "Design and Evaluation of a Screen CCD Imaging System," to be published in *Optical Engineering.*

W. Seka, D. Fried, J. D. B. Featherstone, and S. F. Borzillary, "Light Deposition and Thermal Response in Dental Hard Tissue," to be published in the *Journal of Dental Research.*

L. Shi, T. Gong, W. Xiong, X. Weng, R. Sobolewski, and P. M. Fauchet, "Femtosecond Optical Spectroscopy in Partially Deoxygenated Y-Ba-Cu-O Thin Films," to be published in *Ultrafast Phenomena, IX.*

H. Shi and S.-H. Chen, "Novel Glassy Nematic and Chiral Nematic Oligomers Derived from 1,3,5-Cyclohexane-tricarboxylic and (1R,3S)-(+)-Camphoric Acids," to be published in *Liquid Crystals*.

H. Shi and S.-H. Chen, "Novel Glass-Forming Liquid Crystals. 2. Systems Containing High Optical Birefringence Moiety 1-(Phenyl)-2-(6-Cyanonaphth-2-yl)Ethyne," to be published in *Liquid Crystals*.

M. D. Skeldon, A. Okishev, S. A. Letzring, W. R. Donaldson, and W. Seka, "Optically Activated Switches for the Generation of Complex Electrical Waveforms with Multigigahertz Bandwidth," to be published in *Optically Activated Switching IV*.

R. Sobolewski and T. Y. Hsiang, "Progress in Ultrafast Superconducting Electronics," to be published in the *Proceedings of the International Workshop on Superconductivity and Particle Detection* (invited).

C. J. Twomey, S.-H. Chen, T. Blanton, A. W. Schmid, and K. L. Marshall, "Solid Polymers Doped with Rare Earth Metal Salts. II. Thermal Behavior and Morphology of the Neodymium Acetate-Poly(Ethylene Oxide) System," to be published in the *Journal of Polymer Science, Polymer Physics Edition*.

C.-C. Wang, M. Currie, S. Alexandrou, and T. Y. Hsiang, "Ultrafast, All-Silicon Light Modulator," to be published in *Optics Letters*.

M. D. Wittman, R. Q. Gram, H. Kim, C. K. Immesoete, S. G. Noyes, and S. Scarantino, "Increased Retention Time for Hydrogen and Other Gases by Polymer Shells Using Optically Transparent Aluminum Layers," to be published in the *Journal of Vacuum Science and Technology*.

W. Xiong, W. Kula, R. Sobolewski, and J. R. Gavaler, "Laser Writing: A New Technique for Fabrication of Electronic and Optoelectronic Y-Ba-Cu-O Devices and Circuits," to be published in *SPIE Vol. 2160: Superconductive Devices and Circuits*.

B. Yaakobi, Q. Su, F. J. Marshall, and R. Epstein, "Monochromatic Backlighting as a Laser-Fusion Diagnostic," to be published in the *Journal of X-Ray Science and Technology*.

B. Yaakobi, F. J. Marshall, R. Epstein, and Q. Su, "New Diagnostic Features in the Laser Implosions of Argon-Filled Targets," to be published in *Optics Communications*.

X. Zhou, S. Alexandrou, and T. Y. Hsiang, "Monte Carlo Investigation of the Mechanism of Subpicosecond Pulse Generation by Nonuniform Gap Illumination," to be published in *Applied Physics Letters*.

J. D. Zuegel and W. Seka, "Direct Measurements of Lower-Level Lifetime in Nd:YLF," to be published in the *Bulletin of the American Physical Society*.

Conference Presentations

The following presentations were made at the Materials Research Society Spring '94 Meeting, San Francisco, CA, 4–8 April 1994:

S. D. Jacobs, A. L. Rigatti, D. J. Smith, L. D. Lund, H. M. D'Alessandro, K. L. Marshall, and A. W. Schmid, "Design and Manufacture of Laser Quality Liquid Crystal Optics." (invited)

E. M. Korenic and S. D. Jacobs, "Selective Reflection Properties of Embedded Pre-Aligned Cholesteric Domains as Functions of Incident Angle."

J. C. Mastrangelo and S.-H. Chen, "Thermotropic Side-Chain Polymers Carrying High Optical Birefringence Nematogenic Group."

H. Shi and S.-H. Chen, "Novel Glassy Nematic and Chiral Nematic Oligomers Derived from 1,3,5-Cyclohexanetricarboxylic and (1R,3S)-(+)-Camphoric Acids."

L. Shi, T. Gong, W. Xiong, X. Weng, R. Sobolewski, and P. M. Fauchet, "Femtosecond Optical Spectroscopy in Partially Deoxygenated Y-Ba-Cu-O Thin Films," Ultrafast Phenomena Ninth International Meeting, Dana Point, CA, 1–5 May 1994.

The following presentations were made at the APS 10th Annual High-Temperature Plasma Diagnostics, Rochester, NY, 8–12 May 1994:

T. R. Boehly, R. S. Craxton, R. J. Hutchison, J. H. Kelly, T. J. Kessler, S. A. Kumpan, S. A. Letzring, R. L. McCrory, S. F. B. Morse, W. Seka, S. Skupsky, J. M. Soures, and C. P. Verdon, "The Upgrade to the OMEGA Laser System."

D. K. Bradley, P. M. Bell, O. L. Landen, J. D. Kilkenny, and J. Oertel, "Development and Characterization of a Pair of 30-40 ps X-Ray Framing Cameras."

P. A. Jaanimagi, R. C. Elton, B. L. Welch, Y. Leng, and H. R. Griem, "Extending X-Ray Streak Camera Operation to VUV Wavelengths."

J. P. Knauer, R. L. Kremens, M. A. Russotto, and S. Tudman, "Using Cosmic Rays to Monitor Large Scintillator Arrays."

R. L. Kremens, M. A. Russotto, and S. Tudman, "Performance Simulations of the MEDUSA Neutron Detector."

S. A. Letzring, "Laser and Plasma Diagnostics for the OMEGA Laser System." (invited)

F. J. Marshall and B. Yaakobi, "Quantitative Measurements with X-Ray Microscopes in Laser-Fusion Experiments."

B. Yaakobi, R. Epstein, Q. Su, F. J. Marshall, and D. Shvarts, "Target Imaging and Backlighting Diagnostic on the OMEGA Upgrade."

B. Yaakobi, F. J. Marshall, R. Epstein, D. K. Bradley, P. A. Jaanimagi, and Q. Su, "New Diagnostic Features in the Laser Implosions of Argon-Filled Targets."

The following presentations were made at CLEO '94, Anaheim, CA, 8–13 May 1994:

S. Alexandrou, C.-C. Wang, M. Currie, R. Sobolewski, and T. Y. Hsiang, "Terahertz Spectral Analysis of Straight and Bent Coplanar Transmission Lines."

X. D. Cao, G. P. Agrawal, and D. D. Meyerhofer, "Optimization of Optical Beam Steering in Nonlinear Kerr Media Via Spatial Phase Modulation."

C. Y. Chien, G. Korn, J. S. Coe, X. Liu, J. Squier, G. Mourou, R. S. Craxton, and J.-C. Kieffer, "High-Efficiency Frequency Doubling of Ultra-High Intensity Nd: Glass Laser Pulses."

J. H. Kelly, T. R. Boehly, D. L. Brown, and M. D. Tracy, "The Upgrade to the OMEGA Laser System: A Status Report." (invited)

A. Okishev, M. D. Skeldon, and W. Seka, "Optical Pulse Compression by Stimulated Scattering for Pulse-Shaping Applications in the OMEGA Upgrade Laser."

L. Zheng and D. D. Meyerhofer, "A Linear Cross-Correlation Technique for Single-Shot Measurements of Weak Light Pulses."

The following presentations were made at IQEC '94, Anaheim, CA, 8–13 May 1994:

D. D. Meyerhofer, J. Chaloupka, and J. Peatross, "High-Harmonic Generation with an Annular Laser Beam."

C. I. Moore, J. P. Knauer, and D. D. Meyerhofer, "Observations of Ponderomotively Accelerated Electrons from the Focus of a Very-High-Intensity Laser."

R. A. London, R. P. Ratowsky, A. L. Osterheld, and R. S. Craxton, "Complete X-Ray Laser Modeling: Hydrodynamics, Kinetics, and Optics," 4th International Colloquium on X-Ray Lasers, Williamsburg, VA, 16 May 1994.

The following presentations were made at the 24th Annual Anomalous Absorption Conference, Pacific Grove, CA, 5–10 June 1994:

U. Alon, J. Hecht, D. Ofer, D. Mukamel, and D. Shvarts, "Bubble-Competition Model for Hydrodynamically Unstable Interfaces."

R. Betti, V. Goncharov, R. L. McCrory, E. Turano, and C. P. Verdon, "Cutoff Wave Numbers of the Incompressible Ablative Rayleigh-Taylor Instability."

A. Chirokikh, W. Seka, R. E. Bahr, R. S. Craxton, R. W. Short, A. Simon, and M. D. Skeldon, "Stimulated Brillouin Scattering at 1 μm in Long-Scale-Length Laser Plasmas."

R. S. Craxton, M. Dunne, O. Willi, and T. Afshar-Rad, "Simulations of Soft X-Ray Generated Plasmas Created to Enhance Thermal Smoothing."

J. A. Delettrez, "An Interactive Mix Model in *LILAC* for Linear and Near-Linear Regimes of the Rayleigh-Taylor Instability."

E. M. Epperlein, R. W. Short, and A. Simon, "Ion Thermal Conductivity and Viscosity for Plasmas with Light and Heavy Ions."

E. M. Epperlein and R. W. Short, "Nonlocal Electron Transport in the Presence of High-Intensity Laser Irradiation."

R. Epstein, S. Skupsky, and C. P. Verdon, "Smoothing of Laser Irradiation of ICF Targets Using Pre-Formed Refracting Atmospheres with Small-Scale Inhomogeneity and Time Dependence."

J. Hecht, D. Ofer, U. Alon, T. Tlusty, D. Shvarts, C. P. Verdon, R. L. McCrory, and S. A. Orszag, "Three-Dimensional Simulation of the Late Nonlinear Stage of the Rayleigh-Taylor Instability."

T. Kolber, C. J. McKinstrie, R. Betti, and R. E. Giacone, "Numerical Simulations of Two-Dimensional Stimulated Brillouin Scattering."

J. S. Li, C. J. McKinstrie, C. Joshi, and K. Marsh, "Thermal Filamentation of Counterpropagating Laser Beams."

C. J. McKinstrie, R. Betti, R. E. Giacone, T. Kolber, and J. S. Li, "Two-Dimensional Stimulated Brillouin Scattering."

D. D. Meyerhofer, H. Chen, J. A. Delettrez, E. M. Epperlein, Y. Fisher, and B. Soom, "Flux Limiter in Picosecond Laser-Plasma Interactions."

D. Ofer, U. Alon, D. Shvarts, C. P. Verdon, and R. L. McCrory, "A Modal Model for the Nonlinear Evolution of Multimode Rayleigh-Taylor Mixing Zone."

R. W. Short and E. M. Epperlein, "Generalized Fluid Models for Laser-Irradiated Plasmas."

A. Simon and R. W. Short, "Stimulated Scattering from Low-Frequency Modes in Laser-Produced Magneto-Plasmas."

C. T. Cotton, "The Design of an All-Spherical, Three-Mirror, Off-Axis Telescope Objective," International Optical Design Conference, Rochester, NY, 6–9 June 1994.

M. J. Cumbo, D. Fairhurst, S. D. Jacobs, and B. E. Puchebner, "The Effect of Chemically Modulated Surface Charge in the Polishing of Optical Glass," OSA Science of Finishing (1994), Rochester, NY, 6–8 June 1994.

The following presentations were made at the OSA Optical Fabrication and Testing Workshop, Rochester, NY, 7–9 June 1994:

P. D. Funkenbusch, Y. Y. Zhou, C. Lohnes, D. J. Quesnel, S. D. Jacobs, B. E Puchebner, D. Golini, and A. Lindquist, "Deterministic Microgrinding of Glass with Polycrystalline Diamond Tools."

W. I. Kordonsky, I. V. Prokhorov, B. E Kashevsky, S. D. Jacobs, B. E. Puchebner, Y. Hsu, D. Pietrowski, and D. Stafford, "Basic Properties of Magnetorheological Fluids for Optical Finishing."

W. I. Kordonsky, I. V. Prokhorov, S. D. Jacobs, B. E. Puchebner, Y. Hsu, D. Pietrowski, and D. Stafford, "Glass Polishing Experiments Using Magnetorheological Fluids."

W. Ng, B. E. Puchebner, and S. D. Jacobs, "Evaluation of Bound Abrasive Media for Fabrication of Ring Tool Polishers."

B. E. Puchebner, A. Feltz, W. Ng, and S. D. Jacobs, "Coolant Performance in Bound Diamond Ring Tool Grinding of K7 Optical Glass."

B. E. Puchebner, A. Feltz, and S. Patterson, "The Effect of Additives in a Commercial Coolant on the Glass Grinding Process."

B. E. Puchebner, "Chlorofluorocarbons in the Workplace: A Summary of Guidelines and Alternatives."

E. M. Korenic, "Fractured Cholesteric Liquid Crystal Polymers," UNY-VAC American Vacuum Society Annual Meeting, Rochester, New York, 9 June 1994.

UNIVERSITY OF
ROCHESTER